Magnetotransport in Transition Metal Dichalcogenide Semimetals

by

Archana Tiwari

A thesis
presented to the University of Waterloo
in fulfillment of the
thesis requirement for the degree of
Doctor of Philosophy
in
Physics and Astronomy

Waterloo, Ontario, Canada, 2021

Examining Committee Membership

The following served on the Examining Committee for this thesis. The decision of the Examining Committee is by majority vote.

External Examiner:	Thomas Szkopek Professor, Dept. of Electrical and Computer Engineering, McGill University
Supervisor(s):	Adam Wei Tsen Assistant Professor, Dept. of Chemistry, University of Waterloo
Internal Member:	Raffi Budakian Professor, Dept. of Physics and Astronomy, University of Waterloo
Internal-External Member:	Jonathan Baugh Associate Professor, Dept. of Chemistry, University of Waterloo
Other Member(s):	Dmitry Pushin Assistant Professor, Dept. of Physics and Astronomy, University of Waterloo

Author's Declaration

This thesis consists of material all of which I authored or co-authored: see Statement of Contributions included in the thesis. This is a true copy of the thesis, including any required final revisions, as accepted by my examiners.

I understand that my thesis may be made electronically available to the public.

Statement of Contributions

NOTE: Supervision and contribution from Prof. Adam Wei Tsen (AWT) should be assumed in all of the below.

1. Chapter 3

    - Archana Tiwari (AT) and Shazhou (Joey) Zhong (SZ) fabricated the samples.
    - SZ and AT performed the transport measurement.
    - SZ, AT and AWT analysed the data.

2. Chapter 4

    - AT and AWT conceived the idea and designed the experiment. AT fabricated the devices and performed the transport measurements.
    - Fangchu Chen and Jingjing Gao grew and characterized the $MoTe_2$ crystals under the guidance of Xuan Luo and Yuping Sun.
    - SZ performed the finite element method simulations.
    - Elizabeth Drueke and Austin Kaczmarek performed the optical second harmonic generation measurements under the guidance of Liuyan Zhao.
    - Jahyun Koo performed the density functional theory calculations under the guidance of Binghai Yan.
    - AT and AWT analyzed the data together with Cong Xiao and Qian Niu.

These work are published as

- Chapter 3: Shazhou Zhong, Archana Tiwari, George Nichols, Fangchu Chen, Xuan Luo, Yuping Sun, and Adam W. Tsen. "Origin of magnetoresistance suppression in thin γ-$MoTe_2$." Phys. Rev. B 97, 241409(R) (2018).

- Chapter 4: Archana Tiwari, Fangchu Chen, Shazhou Zhong, Elizabeth Drueke, Jahyun Koo, Austin Kaczmarek, Cong Xiao, Jingjing Gao, Xuan Luo, Qian Niu, Yuping Sun, Binghai Yan, Liuyan Zhao, Adam W. Tsen. "Giant c-axis nonlinear anomalous Hall effect in T_d-$MoTe_2$ and WTe_2." Nature Communications 12, 2049 (2021).

Abstract

In this thesis, we study the large magnetoresistance in $MoTe_2$, and non-linear anomalous Hall effect in $MoTe_2$ and WTe_2. The main results of the thesis are reported in two chapters, each of which is dedicated to different physical observations, as described below.

Thin flakes cleaved from layered single crystals exhibit high mobility, and semimetals show nearly compensated electron and hole density. The two combined in a layered semimetallic TMDC show a large and unsaturated magnetoresistance. However, thinning down the sample to a few atomic layers results in a charge imbalance and a decreased mobility, suppressing the overall magnetoresistance. As large magnetoresistance is an important component of various applications, it is important to determine which of these factors are prominent in affecting the magnetoreistance in the thin materials, and potentially modify that factor for 2D XMR applications. To study this, we use thickness tuned magnetotransport measurements on a semimetallic layered TMDC, $MoTe_2$. We use a two-band model to extract mobility and electron-hole ratio from the magnetoresistance measurements. Upon analysing the data over various thicknesses, we conclude that the suppression of magnetoresistance in thin layers is prominently impacted by the mobility. A high mobility in thin layers can be achieved by using a high quality single crystals and providing an atomically flat substrate of boron nitride for device fabrication. We also measure Shubnikov de-Haas (SdH) oscillations in the resistivity of $MoTe_2$ at high magnetic field. We analysed the frequency of these oscillations in the inverse of magnetic field to find corresponding signatures of electron and hole pockets on the Fermi surface.

The other phenomena we try to explore is the anomalous Hall effect(AHE) in a time reversal invariant system. AHE originates both from the Berry curvature mechanism intrinsic to the material, and spin-orbit coupled impurity scattering processes. A non-zero Berry curvature requires the system to be breaking either of the time-reversal(TRS) or inversion symmetries. While the AHE in TRS breaking ferromagnetic materials has been elaborated upon in literature, a general theory of AHE in IS breaking materials was only recently provided. For inversion symmetry breaking systems, the Hall effects appears as a DC and second harmonic response to the applied current, giving a non-linear anomalous Hall effect (NLAHE). Three dimensional TMDCs, $MoTe_2$ and WTe_2, are non-centrosymmetric crys-

tals, where application of in-plane electric field gives a finite NLAHE along the c-axis. For measurements, we designed a device with both in-plane and vertical contacts to measure the first and second harmonic responses. To parse different contributions to the NLAHE, we rely on the scaling relation between the NLAHE strength and longitudinal conductivity. We provide a scaling with conductivity by changing the thickness and temperature. Our scaling relation shows that the NLAHE is dominated by skew scattering contribution along with a new exponential dependence on conductivity at low temperatures. Finally, to put this work in context with the existing AHE results, we measure the Hall ratio and Hall conductivity.

Acknowledgements

The time spent during my PhD was filled with learning experiences, thanks to the people I have interacted with on both professional and personal front.

I would first like to thank my supervisor Prof. Adam Wei Tsen for teaching me the methodologies of experimental research, collaboration, and time management. I would like to thank the members of my defence committee for critically reading this thesis and providing their comments. We were a new research group when I was starting my PhD, therefore, every lab member played a vital role into establishing and taking care of lab facilities. For this, I would like to thank past and present members of our lab, Hyun Ho Kim, Tarun Patel, Joey Zhang, Bowen Yang and Tina Dekker. We were able to make good quality samples thanks to the crystals grown by Fangchu Chen and members of Prof. Yuping Sun's group. I have learnt a great deal of nanofabrication thanks to the multiple discussions with Eduardo Berrera, Francois Sfigakis, and members of quantum nanofabrication team at the Quantum Nano Center. I would also like to thank Prof. Jonathan Baugh and Prof. David Cory, and members of their group, especially, Peter, George, and Francois for accommodating us with their measurement facilities before our lab became fully functional. I am grateful to Prof. Anton Burkov for furthering my understanding of condensed matter physics through a course on "Current Topics in Condensed Matter Physics." I would also like to thank the administration at Research Advancement Center, Chris and Harmeny for providing a comfortable working environment.

On personal front, I would first like to thank my brother Ravish for his constant support, without whom I will have to rethink various aspects of my life. I would like to thank Meenu, Dennis, Sreesh, Raghav, Hemant K. & S., Sayandip and Priya, for providing a safe space to open up, and extending their support. Thanks to Rahul, Pavithran, Tarun, Zeeshan, Harshita, Retnika, Sharath, Abhinav and Jimit for being a part of my journey here.

Finally, to my parents, my dad who instilled my initial interest in sciences. It is him from whom I have learned my most basic lessons of science, mathematics and life, and my mom for her care and support. To my siblings, Deepika and Shreyansh, for taking care of responsibilities at home while I'm away.

Dedication

This is dedicated to my parents.

Table of Contents

List of Figures

List of Tables

Chapter 1

Introduction

The last decade has seen a dramatic shift in the experimental approach to the condensed matter physics with the isolation of atomically thin Graphene by Geim and Novoselov in 2004 [4, 5]. Their technique of mechanically isolating mono- or few-atomic layers from a bulk crystal, combined with a large library of layered crystals, has enabled exploration of both fundamental physical properties and novel device functionalities. A further development to form heterostructures with pristine interfaces, where electrons are exposed at the interface of different materials, has lead to emergence of new quantum properties. For instance, heterostructure assembly into moiré patterns for bilayer graphene twisted at certain angles exhibit superconductivity [6], and emergent ferromagnetism [7]. Graphene/BN moiré heterostructure have shown Chern insulator characteristics, originating from correlation effect and emergent paramagnetism in each lattice [8].

Transition metal dichalogenides (TMDCs) are another class of layered crystals with interesting electronic properties. TMDC semimetals, $MoTe_2$ and WTe_2, are non-centrosymmetric crystals with large spin orbit coupling and high mobility. These properties have lead to the observation of large magnetoresistance [9, 10, 11], predictions of type-II Weyl semimetal [12, 13, 14], large spin orbit coupling [15, 16], superconductivity [17, 18], and edge states [19, 20, 21].

In this thesis, we will investigate an interplay between the crystal structure and transport properties of layered transition metal dichalcogenides. In particular, we study thick-

ness evolution of large magnetoresistance in $MoTe_2$, and crystal symmetry dependent non-linear Hall like effects in $MoTe_2$ and WTe_2.

1.1 Two dimensional materials

There was a long held belief backed by both theory [22, 23] and experiments that two dimensional materials cannot exist in a free standing form. Theoretically, it was suggested that at any finite temperature the thermal fluctuations can reach to the length scale of interatomic distance making the system unstable [24]. Experimentally, it was shown that a decrease in the melting point of film upon decreasing the thickness can decompose it at typically dozens of atomic layers [25, 26]. Therefore, conventionally, thin films were grown on a 3D lattice matching substrate by the bottom-up approach of Molecular Beam Epitexy and Chemical Vapour Deposition. These conventional methods provide a benefit of large area growth but require special equipment which are expensive and time consuming. The resultant film and heterostructure have grain boundaries, and may have a strained or charge trapped interface.

Two dimensional (2D) materials are single atomic layers of materials with thickness ∼0.5-0.7nm. This dimensional confinement has consequences on the density of states, symmetry properties, and spin-orbit interactions. In layered materials, in-plane bonds are covalent (∼10 eV/atom) in nature, and out-of-plane bonds are of van der Waals type (∼30-60 meV/atom), close to the thermal energy at room temperature ∼26 meV. Presence of weak van der Waals force allows for mechanical isolation of thin layers of material using a scotch tape. Furthermore, layered 2D materials host various electronic and structural phases, even a single system can exhibit more than one phase under various conditions of thickness, strain, defects, temperature, magnetic field, and gating.

1.1.1 Graphene

Graphene is an arrangement of sp^2 hybridized carbon atoms in a hexagonal lattice. Three of the four valence electron orbitals are sp^2 hybridized to form a σ bond, and an unpaired

electron in the p_z orbital forms π bond with the neighbouring carbon atoms. The in-plane σ and out-of-plane π bonds are responsible for robust in-plane bonding in carbon allotropes and transport properties in Graphene, respectively.

Fig. 1.1 shows the lattice structure of Graphene, the two carbon atom basis unit cell has a lattice constant, $a = |a_1| = |a_2| = \sqrt{3} \times 1.42 = 2.46\mathring{A}$. The strong σ bond allows electrons to be tightly bound with each carbon site while π bond gives contribution to the hopping term, allowing applicability of tight binding model based analysis. The eigenfunction corresponding to the Hamiltonian of a single atom gives the atomic orbital function, and the crystal potential acts as a perturbation field resulting into modified atomic orbital in the form of Bloch wave function.

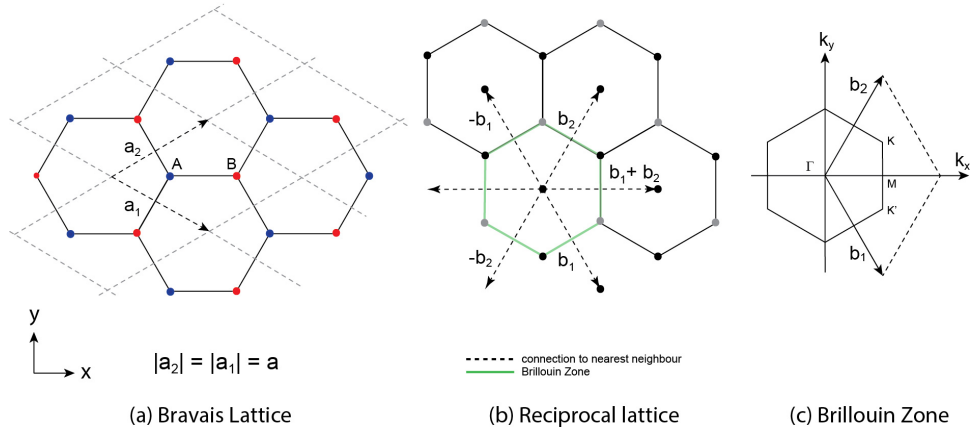

Figure 1.1: The lattice and reciprocal lattice structure of graphene. (a) Bravais lattice of graphene made from the unit cell (dashed parallelogram) consisting of two carbon atoms. (b) Reciprocal lattice and construction of Brillouin zone. (c) Brillouin zone with high symmetry k-space points.

The resulting dispersion relation is equation 1.1, where t is the hopping term. Fig. 1.2 shows the linear dispersion relation at low energy, high symmetry K and K$'$ points host massless Dirac particles and have low density of states. The saddle points in between the K and K$'$ have high density of states, formation of moiré structure with bilayer Graphene

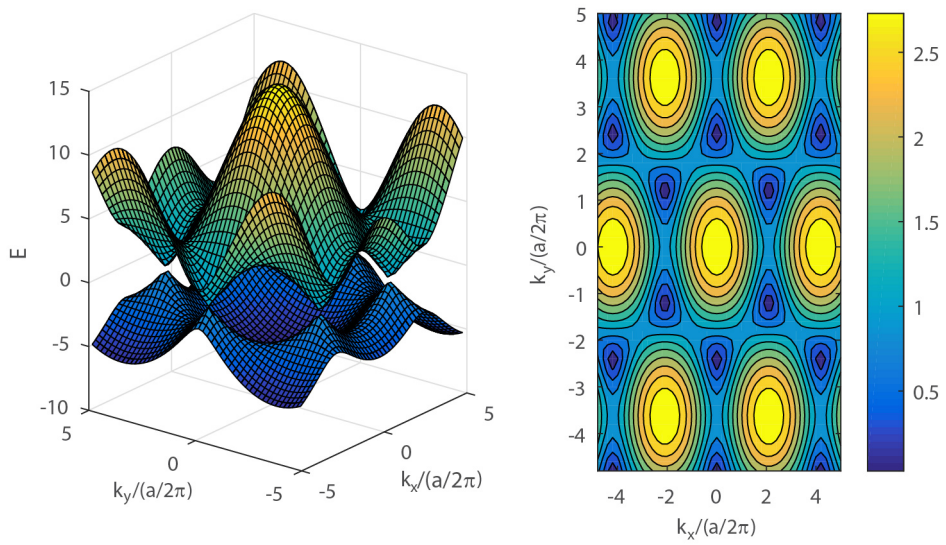

Figure 1.2: Energy dispersion relation of Graphene. (a) Conduction and valence band in Graphene touching at K and K$^{'}$ points. (b) Contour plot with projection on K_x-K_y plane depicting the hexagonal Brillouin zone.

modulates the energy for saddle points [6].

$$E(k_x, k_y) = \pm t\sqrt{1 + 4\cos\frac{\sqrt{3}k_x a}{2}\cos\frac{k_y a}{2} + 4\cos^2\frac{k_y a}{2}} \tag{1.1}$$

Hexagonal Boron Nitride

Boron nitride (BN) is an isomorph of graphene where adjacent C-sites are replaced by B and N atoms. Since the energy at the B and N sites are different, it breaks the inversion symmetry of the system. A large difference between the electronegativity of B and N atoms leads to a wide bandgap of 5.76 eV [27], the dispersion relation for BN is given in the equation 1.2. It is also chemically inert, therefore, can be used as an encapsulation

layer to protect sensitive materials from degradation in air.

$$E(k_x, k_y) = \frac{(\varepsilon_B + \varepsilon_N)}{2} \pm \sqrt{\frac{(\varepsilon_B - \varepsilon_N)^2}{2} + t^2 + 4t^2 \cos\frac{\sqrt{3}k_x a}{2} \cos\frac{k_y a}{2} + 4t^2 \cos^2\frac{k_y a}{2}} \quad (1.2)$$

1.1.2 Transition Metal Dichalcogenides

Transition metal dichalcogenides (TMDCs) have a general formula of MX_2, where a transition metal element (M= group 4-6 and 10) is sandwiched between two layers of chalcogen atoms (X= S, Se, Te). The intra-layer bond between M and X atoms are covalent in nature, while inter-layer bond between each MX_2 layer is of van der Waals type. Each metal atom in MX_2 is bonded with 6 chalcogen atom, and each chalcogen atom is bonded with 3 metal atoms, giving the oxidation state for metal (M) and chalcogen (X) as +4 and -2, respectively. Their electronic properties depend on the specific choice for atoms (M,X) and their relative arrangement. A detailed list of properties with different transition metals is given in the Table 1.1. TMDCs crystallize in 2H, 3R, 1T, and 1T$'$ structures, where digits indicate the number of X-M-X layers in a stacking sequence. 1T has octahedral while 2H and 3R have trigonal prismatic coordination as shown in Fig. 1.3. Most common electronic phases among TMDCs are semiconducting 2H and semimetallic 1T phases.

M	X	Properties
Ti, Hf, Zr	S, Se, Te	Semiconducting, Diamagnetic
V, Nb, Ta	S, Se, Te	Metals, Supercondcutor, Charge Density Wave
Mo, W	S, Se, Te	Semiconducting, Semimetallic
Tc, Re	S, Se, Te	Semiconductor, Diamagnetic
Pd, Pt	S, Se, Te	Semiconducting, metallic, Superconducting

Table 1.1: Electronic properties of TMDC materials. Adopted from [3].

Many of the semiconducting TMDCs have a band gap of 1-2 eV [28] which changes from indirect to direct band gap with decreasing thickness. 2H-MoS_2 is a typical example of this transition [29], where an indirect bulk band gap of 1.2 eV changes into direct 1.9 eV of band gap in monolayer as shown in Fig. 1.4 due to quantum confinement.

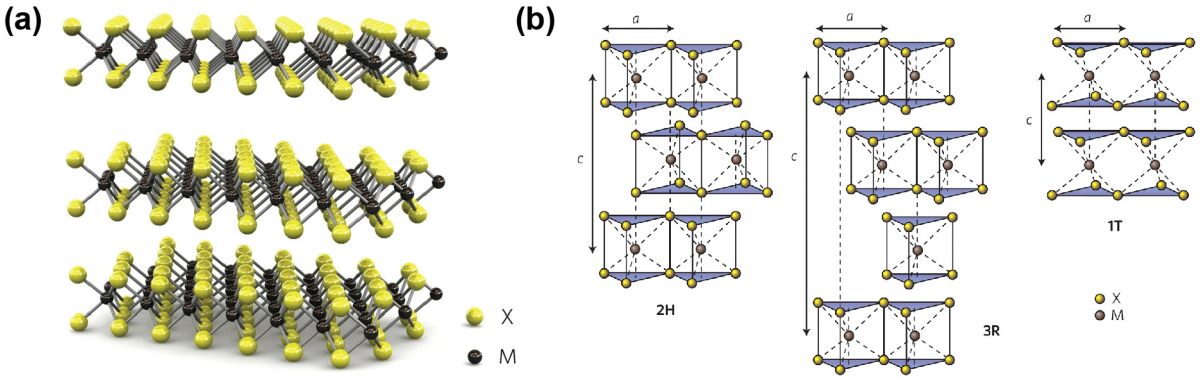

Figure 1.3: MX_2 stacking in a typical TMDC. (a) 3D stacking of M(grey) and X(yellow) atoms. (b) Polymorphs of TMDCs from left to right: 2H, 3R, 1T. Reproduced from [30].

Upon decreasing the thickness, transitions at Γ point shift significantly from an indirect to direct band gap. Other semiconducting TMDCs, $MoSe_2$, 2H-$MoTe_2$ and WSe_2 and their heterostructures have also been investigated for their layer dependent band structure contributing to optoelectronic properties.

M(Mo, W)Te_2

True 1T coordination is unstable in $MoTe_2$ as in-plane bond distortions dimerize the Mo atoms along the b-axis. Two stacking configurations of these distorted layers along the c-axis give rise to distinct three-dimensional (3D) structures: the centrosymmetric β (or 1T') phase at high temperature (above ∼250K) and the noncentrosymmetric γ (or T_d) phase at low temperature, with the difference being only a ∼4° tilt in the unit cell. The orthorhombic non-centrosymmetric phase belongs to the space group $Pmn2_1$, it hosts type-II Weyl nodes which is characterized by linear touching between electron and hole pockets [31, 32, 33, 34, 35, 13, 36]. Given to the high mobility and charge compensation, they exhibit extremely large magnetoresistance (XMR) below ∼20K [9, 10, 37]. Fig. 1.5 shows the crystal structure of 1T $MoTe_2$ and its structurally distorted phases.

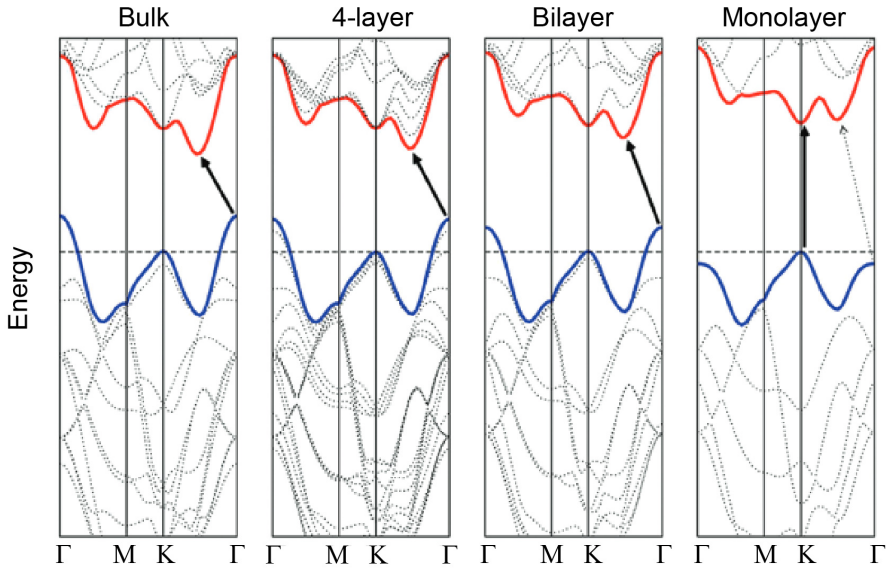

Figure 1.4: Indirect to direct band gap transition in 2H-MoS_2 with reducing number of layers with a band gap of 1.2 eV and 1.9 eV, for bulk and monolayer, respectively. Reproduced from [1].

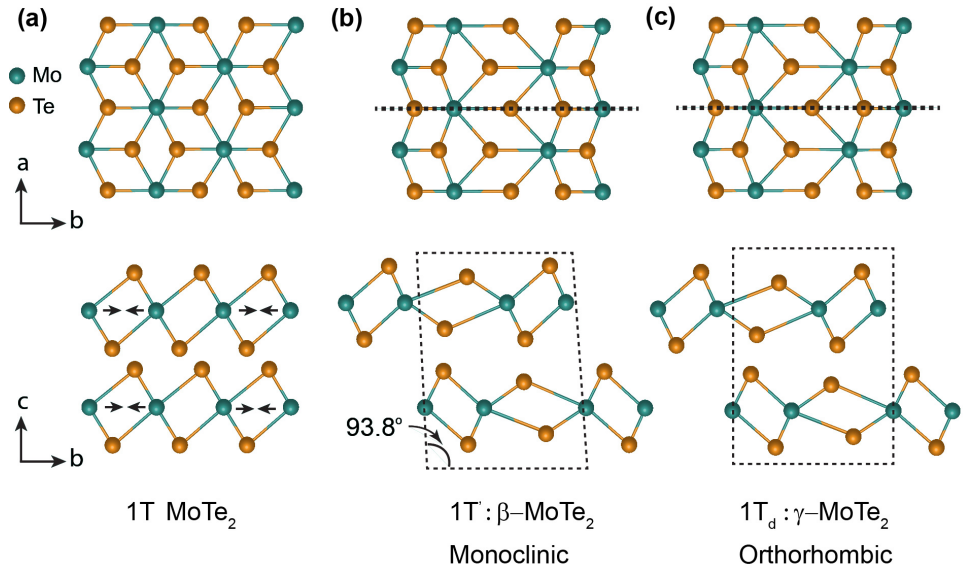

Figure 1.5: Phases of 1T $MoTe_2$, with atomic arrangement along in-plane (top row) and out-of-plane (bottom row) direction. (a) Unstable 1T phase where Mo atoms dimerizes into 1T$'$. (b) Tilted unit cell for the distorted high temperature β-$MoTe_2$. With black line depicting the mirror symmetry along a-axis. (c) γ-$Mote_2$ stabilizes at low temperature or low thickness.

1.2 Heterostructure

The ease of formation of heterostructures is one of the most attractive capabilities of layered materials. Heterostructures are formed by co-lamination and restacking of layers of different materials. Constituent layers can be stacked in different sequences and angles to achieve a certain functionality. These functionalities range from intrinsic material property of changing the band structure to extrinsic factors of providing a flat substrate and encapsulation from the environment, creating a tunnel junction, dielectric barriers and acting as a contact electrodes. Since the constituent layers also support van der Waals interactions in their native crystal, it excludes the requirement of lattice matching. Viscoelestic polymers are used to sequentially pick-up and transfer material layers from one substrate to another to form a multilayer structure.

One of the recent developments on the formation of moiré patterns by angle dependent stacking of monolayers have caused emergence of new electronic phases [38, 39]. The key theoretical insights were given by Bistritzer and MacDonald that for a moiré stacking, nearest neighbour site for hopping of the electron can come from the adjacent layer. Therefore, controlling the twist angle can change velocity of Dirac points, density of states, and at a precise magic angle of 1.05°C causes flattening of lowest energy bands in graphene [38]. Experimentally, it can be achieved by tearing off a section of a material sheet, then align it with the base sheet at a precise angle [6, 40].

1.3 Thesis Overview

This thesis entails study of devices based on layered TMDCs: $MoTe_2$ and WTe_2. We first investigate the thickness-tuned evolution of electronic structure for a low temperature phase of $MoTe_2$ (T_d-$MoTe_2$). Then, we study the space group symmetry of T_d-$MoTe_2$ and WTe_2, and corresponding non-linear phenomena using second harmonic measurements.

In chapter 2, we discuss the standard experimental techniques for fabrication and measurement of layered material based devices. We include details on mechanical exfoliation, polymer assisted heterostructure assembly, and fabrication of contact electrodes. The

methods for device fabrication and measurements will be used in chapters 3 and 4.

In chapter 3, we study large magnetoresistance of T_d-$MoTe_2$. We focus on the thickness evolution of large magnetoresistance in a semimetallic phase of $MoTe_2$. We perform magnetotransport measurements and assess electronic transport by using a two-band model. We measure quantum oscillations in $MoTe_2$. The frequency obtained from the quantum oscillations are used to identify the electron and hole pockets of the Fermi surface.

In Chapter 4, we discuss the symmetry properties of TMDC materials $MoTe_2$ and WTe_2, and its consequences on non-linear transport. We present both first and second harmonic Hall measurements for in-plane and out-of-plane directions of the crystal. To elucidate the mechanism involved in this process, we propose a scaling law with respect to the relaxation time upon varying the temperature, and discuss the impact of asymmetric scattering mechanisms.

Chapter 5 concludes the work presented in this thesis and provides an outlook for future experiments into probing Weyl semimetal and non-linear anomalous behaviour in $MoTe_2$ and WTe_2.

Chapter 2

Experimental Methods

In this chapter, we will talk about device fabrication methods for two dimensional materials based measurements. In particular, we include the details of heterostructure assembly techniques using polymers, and fabrication of contact electrodes.

2.1 Heterostructure Assembly

2.1.1 Mechanical Exfoliation

The van der Waals inter-layer interactions in layered materials are weak enough to allow for their separation at room temperature using a scotch tape. A bulk crystal is first placed onto a scotch tape, after multiple repetitions of sticking and releasing the tape to the crystal, thin layers of the material are separated out. These layers are then transferred to a substrate (Si/SiO_2 or a polymer stamp) for identifying appropriate thickness and shape. To form pristine surfaces and avoid oxidation of sensitive materials, this process is usually carried out inside a nitrogen or argon filled glove box with oxygen and moisture content <2 ppm.

An optical microscope is used for a rough estimation of flake dimension and thickness. The visibility under a microscope depends on the band gap and thickness of the flakes. In

their bulk form, insulators with their high band gap are usually transparent, while semiconductors, depending on their band gap exhibit different colours. In case of mono(few)-layers, a rough estimate of thickness can be made by looking at the contrast of diffracted light from the thin film.

2.1.2 Transfer techniques

With the availability of few(mono)-layers, the next step is to assemble them in a desired heterostructure geometry as per measurement requirements.

There are both wet and dry transfer techniques for creating heterostructures. In this thesis, we use polymer based dry transfer techniques, as they provide cleaner interfaces and are less destructive towards chemically sensitive materials. The required polymer properties for heterostructure assembly are: ability to form a close contact with the material surface, transparent in nature to provide alignment accuracy, temperature dependent elastic properties, and less residue formation.

Polydimethylsiloxane (PDMS) and Polycarbonate (PC) are transparent viscoelastic polymers used in this work. Viscoeleastic materials act as an elastic solid over short timescales, and can slowly flow at longer timescales and temperature. When they are slowly brought in contact with the substrate surface they conform to the materials present on the substrate. Their viscoelastic properties are temperature dependent, and at a low operating temperature of $\sim$70-90°C leave negligible residue during transfer process. Some of the challenges associated with this method are achieving correct alignment with multilayer stacking, and avoiding formation of air bubbles and polymer residue on the material surface.

Polydimethylsiloxane (PDMS) assisted Fabrication

PDMS stamps can be made by curing a solution of Sylgard 184 elastomer or can be purchased as a gelfilm from Gelpak. Thin ($\sim$1mm) PDMS stamps are cut into small 1cm$\times$1cm pieces, and placed onto a glass slide. Scotch tape with exfoliated flakes is then put on top of the stamp and pressed lightly using a smooth surface (i.e. cotton swab) to make a close contact between layered materials and the PDMS surface. Tape is then

ripped off of PDMS surface in a quick horizontal motion, resulting into layers of exfoliated materials of varied thickness and shape on the PDMS stamp. To find out correct thickness and shape, the glass slide along with the PDMS stamp is loaded onto a micromanipulator to be viewed under an optical microscope. This micromanipulator has a motion capability for all three x, y and z-axis, allowing to scan the whole stamp with x-y motion, and focusing on flakes of different thicknesses through z-axis manipulation.

Once we identify a desired thickness and shape for each constituent layer in the heterostrucuture, the PDMS stamp is aligned with the bottom contact electrodes on a Si chip for transferring the material on the substrate. Glass slide with the PDMS stamp facing the substrate is slowly lowered down to make a contact with the substrate at around 60-90°C. PDMS stamp is then retracted from the Si chip, leaving the material on the bottom contact electrode as SiO_2 surface is smooth and flat, and at a high temperature thin flakes have higher affinity for it than polymer surface.

Although PDMS assisted transfer is a straightforward method, picking up and transferring one material at a time, makes it a time consuming process, and leaves residue at the interface of a multi-layer device. Therefore, a better technique would be to use van der Waals force of layered flakes to pick up subsequent layers, then transfer the final stack onto contact electrodes, this can be achieved by PC assisted technique explained in next section.

Polycarbonate (PC) assisted Fabrication

To make a PC film, a drop of Polycarbonate solution with anisole (6%) is spread out on a glass slide and cured for 10 minutes at 90°C forming a thin PC layer. This thin layer is then cut into small pieces to be transferred onto PDMS gel with just allowing a small window($\sim$1mm$\times$1mm) for PC layer. This PDMS/PC stamp then used for picking up layers of different materials. PC film expands upon exposing to a temperature as small as 40°C, and makes a close contact with the material surface, after making the contact temperature is further raised to 70-100°C for enhancing the contact. While retracting the PC to pick up the material(M), it is again cooled down to 40°C. The stack of PDMS/PC/M is then used for picking up other materials to form the heterostructure, once the assembly is complete.

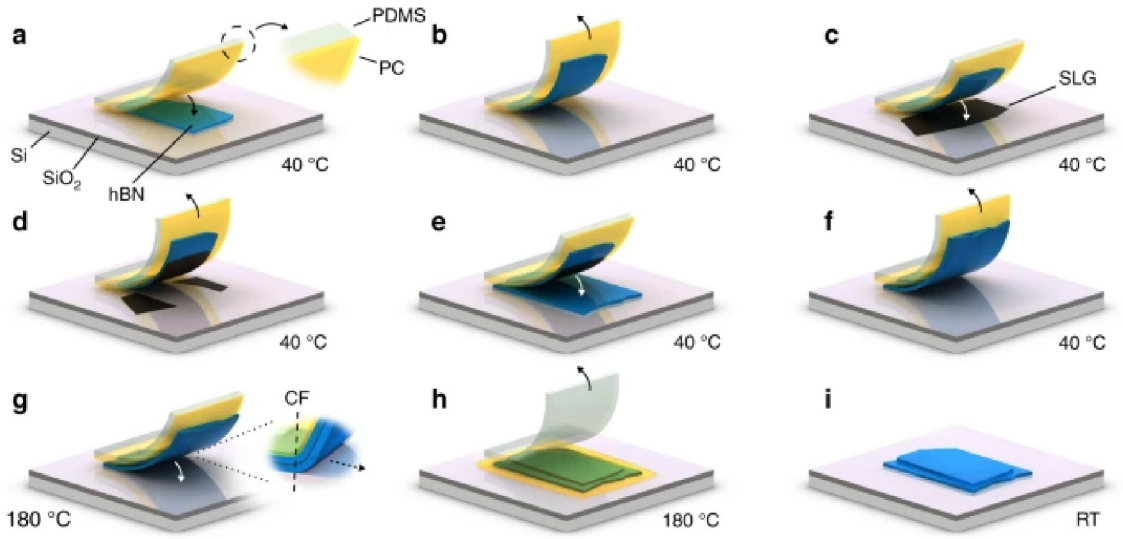

Figure 2.1: PC assisted assembly of BN/Graphene/BN heterostructure. (a)-(b) Picking up of top BN layer on th PC surface (c)-(d) Use of van der Waals interaction to pick-up single layer Graphene (SLG) using PDMS/PC/BN. (e)-(f) Picking up of bottom BN layer to provide complete encapsulation. (g)-(h) Transfer of final stack by melting the PC at 180°C. (i) Final stack after top PC film was dissolved using a chloroform solution. Reproduced from [41].

The whole stack is transferred onto a bottom contact electrode where temperature is raised upto, 150°C to melt the PC film. A typical example of making BN/Gr/BN heterostructure is shown in Fig. 2.1.

2.2 Fabrication of contact electrodes

Contact electrodes are fabricated through a combination of nanofabrication techniques in a clean room environment. The three major components of this process are: (i) coating of a resist layer (ii) exposure to a radiation source and (iii) deposition of a metal

2.2.1 Spin Coating

Spin coating is a method of coating a thin layer of a solution by rotating the substrate at a certain speed. Thickness of the resulting film depends on the molecular weight of the solute, concentration of the solvent and rotating speed of the substrate. For the purpose of lithography, a resist layer is coated onto the substrate.

A resist is a material which is sensitive to the exposure of e-beam(or light) in a lithography process. Thickness of the resist is an essential factor in deciding the resolution of the lithography pattern, and thickness of the metal deposited. Usually, it is recommended to have a resist layer 2-3 times thicker than the deposited metal to avoid cracking of the resist during deposition process. The electron beam resist used in this thesis is Polymethyl methacrylate (PMMA) A6, where A6 represents the 6% of PMMA solutiion in a Anisole. A bilayer resist with MMA/PMMA was used to get a better undercut. Photolithography process in this work uses bilayer PMGI/Shipley 1805 as a photoresist.

2.2.2 Lithography

Lithography in the context of nanofabrication is a transfer of patterns on an e-beam (light)-sensitive material by selective exposure. It is based on the interaction of a radiation source (electron beam or laser) with the underlying polymer resist which either weakens (positive

resist) or strengthens (negative resist) the polymer bonding, allowing it to dissolve or remain intact in a developer solution. The resolution achieved by the patterning devices is based on the wavelength of the radiation, in e-beam lithography it is controlled by the acceleration voltage for electrons.

A resist coated chip is loaded into the chamber for exposure, chamber is brought to a low pressure to reduce the scattering of the beam. Substrate is corrected for its alignment and focus. Then write field alignment is performed to match the sample coordinate with the pattern coordinate in the CAD. After achieving sufficient amount of correction factor the exposure window is opened for patterning.

In this work, we have used Raith150 Two e-beam lithography for making contact electrodes, with 10 keV of accelerating voltage and 30 μm aperture. We used Heidelberg-MLA for the photolithography with 405 nm laser source.

2.2.3 Electron-beam Evaporation

Electron-beam evaporation was used to deposit contact electrodes on Si/SiO_2 substrate. Electrons beams generated by thermionic emission or field effect emission are accelerated towards the deposition metal and upon striking with the material surface lose their kinetic energy converting it to other forms of energy, including thermal energy. This thermal energy then melts the metals, which under sufficient temperature and low pressure sublimes to form vapor, the vapors condenses on the substrate and gets deposited. In our experiments, we used Intlvac Nanochrome II-UHV(10^{-7} torr) beam evaporator with a power of 10keV for depositing gold. Since noble metals have less affinity towards oxygen, it causes poor adhesion on SiO_2 surface, a thin ($\sim$ 5nm) Titanium or Chromium layer is used as an adhesive layer. These electrodes can be used both as a bottom contact or top contact. We have used bottom contact electrodes of Au(45nm)/Ti(5nm).

Atomic Force Microscopy

Atomic force microscopy is based on the mutual interactive forces between two surfaces, namely, the AFM probe and specimen to be measured. The function of AFM is based

on Hooke's law, where cantilever is deflected after reaching very close to the surface. A laser light is shined on the cantilever to track its movement, the deflected laser light from cantilever is collected by a position sensitive detector (PSD) consisting of two photodiodes, signal from PSD is then transferred to a differential amplifier to give final data on surface topology and thickness. It can be used both in contact and non-contact mode, in our experiments, we used Bruker Nanoscope AFM in a nondestructive tapping mode for measurement, it can resolve height difference down to nanometer scale in z-axis.

2.3 Summary

PDMS assisted transfer and e-beam lithography were used to assemble $MoTe_2$/BN heterostructure, and patterning of contact electrodes for the devices in magnetoresistance measurements in chapter 3. The low temperature measurements were conducted in a ^{3}He cryostat, with a magnetic field capability of 12T.

PC based transfer and photolithography techniques were used to assemble heterostructre BN/$MoTe_2$/BN/Gr/BN, and pattern contact electrodes used for non-linear Hall measurements in chapter 4. ^{4}He cryostat was used for low temperature measurements with 14T magnet.

Chapter 3

Linear magnetotransport in $MoTe_2$

In chapter 1, we discussed that layered transition metal dichalcogenides (TMDCs) widen possibilities for understanding both fundamental material properties and innovative device configurations. Their availability in various structural and electronic phases, along with facile phase transition methods, can lend information about electronic transport mechanisms and corresponding physical phenomena. This capability, combined with the experimental methods available for device fabrication and measurement discussed in chapter 2, can play an important role in exploring TMDC material based devices and their applications.

In this chapter, we will talk about $MoTe_2$, an interesting member of TMDC material system, which crystallizes in both semiconducting 2H and semimetallic 1T-type structures. We will investigate the large magnetoresistance exhibited by a low temperature phase (T_d) of 1T-$MoTe_2$. We first give an introduction to the magnetoresistance in non-magnetic materials. We present measurements depicting structural phase transition in $MoTe_2$ with respect to thickness and temperature. We measured a large magnetoresistance in $MoTe_2$ which systematically suppresses upon decreasing the thickness. To understand the implications of tuning thickness on magnetoresistance suppression, we look into the carrier transport properties $MoTe_2$. Thereafter, we use a two band model to quantitatively analyse carrier mobility and carrier density upon changing thickness. Finally, we discuss the results from magnetoresistance measurements and two band model fitting to comment on

the evolution of electronic structure of T_d phase of $MoTe_2$ upon changing thickness.

3.1 Introduction

3.1.1 Magnetoresistance

Magnetoresistance is a change in the electrical resistance of a material upon applying magnetic field, quantified by percentage magnetoresistance (MR), $\frac{\Delta\rho}{\rho} = \frac{\rho(B)-\rho(0)}{\rho(0)}$. Large magnetoresistance (XMR) usually discussed in the context of magnetic materials with Giant magnetoresistance (GMR, MR% $\sim$ 50%) and Colossal magnetoresistance (CMR, MR% $\sim$ 10^5%), have shown applications in spintronics and sensing devices. In non-magnetic metals with isotropic Fermi surface application of magnetic field does not result in a net magnetoresistance. However, a finite MR can be observed in semimetals [9], semiconductors with anisotropic Fermi surface. Fig 3.1 shows a classical picture of an electron transport in a non-magnetic material upon applying magnetic field, deviation in the path of electron reduces the mean-free path and increases the resistivity. The force experienced by an electron moving in a constant magnetic field is given by:

$$\frac{dk}{dt} = -\frac{e}{c}[v \times B] \tag{3.1}$$

corresponding time period of motion in a circular orbit is, $T = 1/\omega_c = \frac{m^* c}{eB}$. This force is perpendicular to the velocity of electron, and the momentum component along the field ($B \parallel z$) is conserved. Therefore, k is confined to the orbital defined by the intersection of Fermi surface with a plane normal to H. For a closed Fermi surface all of such cross-sections are closed orbits while for open Fermi surface some of them can be open orbits.

Semimetals show a large MR at low temperatures as charge compensation leads to near cancellation of Hall electric field. Under charge compensation and weak magnetic field ($\omega_c\tau << 1$) MR varies as μB^2. At large MR saturates to a constant value.

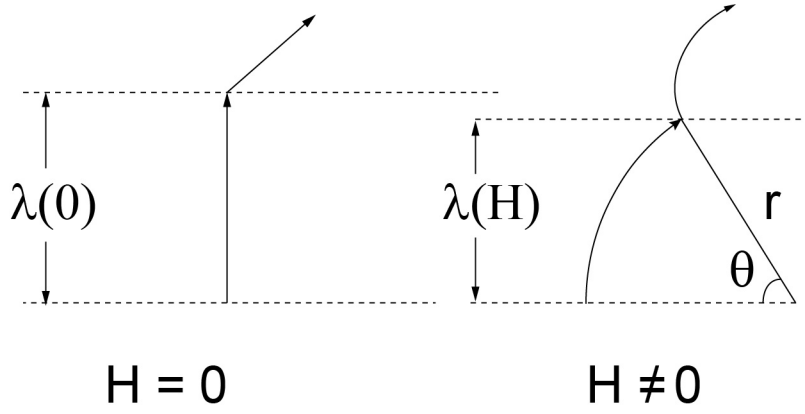

Figure 3.1: A classical picture of electron scattering under magnetic field. The mean free path λ decreases as a result of circular motion caused by magnetic field (H).

Magnetoresistance in the two-band model

Two band model includes contributions from carriers in one hole and electron band only. For the same applied electric field both bands can contribute differently to the overall conductivity.

$$E = \frac{1}{\sigma_i} J_i + \frac{\beta_i}{\sigma_i} H \times J_i \tag{3.2}$$

where σ is the conductivity and R $= \beta/\sigma$ is the Hall coefficient. Taking a cross product with H will give:

$$H \times E = \frac{1}{\sigma_i} H \times J_i + \frac{\beta_i H^2}{\sigma_i} J_i \tag{3.3}$$

Combining both the equations

$$J_i = \frac{1}{1 + \beta_i^2 H^2} (E - \beta_i H \times E) \tag{3.4}$$

Total current from both bands is $J = J_1 + J_2$. Calculating electric field from the total

current:

$$E = \frac{1}{\sigma(1+\beta^2H^2)}(J + \beta H \times J)$$
$$\sigma = \frac{\sigma_1}{1+\beta_1^2H^2} + \frac{\sigma_2}{1+\beta_2^2H^2} \tag{3.5}$$

Magnetoresistance can be written as:

$$\rho = \frac{1}{\sigma(1+\beta^2H^2)} \tag{3.6}$$

For H = 0

$$\rho_0 = \frac{1}{\sigma_1 + \sigma_2} \tag{3.7}$$

Relative change in magnetoresistance can be written as:

$$\frac{\Delta\rho}{\rho_0} = \frac{\rho - \rho_0}{\rho_0} = \frac{\sigma_1\sigma_2(\beta_1 - \beta_2)^2H^2}{(\sigma_1+\sigma_2)^2 + H^2(\beta_1\sigma_1 + \beta_2\sigma_2)^2} \tag{3.8}$$

T_d phase of both $MoTe_2$ and WTe_2, with a distorted crystal structure exhibit an anisotropic Fermi surface, has been shown to demonstrate a large and non-saturating MR [37, 9]. Transport studies have attributed the cause to a close compensation of electron and hole concentrations at low temperature for both the materials [11, 42, 43, 44]; however, angle-resolved photoemission experiments report that $MoTe_2$ remains uncompensated at all temperatures [45], in contrast to WTe_2 [46]. One can directly test the effect of charge (un)compensation on XMR in $MoTe_2$ by changing the relative carrier concentrations, but this is generally difficult to do in bulk systems without introducing unwanted disorder.

It has been shown that the T_d phase is realized in thin $MoTe_2$ samples (below$\sim$12nm) at all temperatures up to 400K [47], potentially allowing for the observation of Weyl nodes and their surface states under ambient conditions. The cause has been attributed to c-axis confinement of the hole bands. For the bulk crystal, it has been calculated that both electron and hole pockets shrink when cooling from the β to γ phase [48], and so it is possible that reducing thickness similarly stabilizes the latter at higher temperatures by confining the hole bands to lower energy.

In principle, these differences for thin samples should have a marked effect on the magnetoresistance (MR) at low temperature, provided that charge compensation is responsible for the XMR. Namely, we expect that a changing electronic structure would alter the delicate carrier balance achieved in the bulk crystal. We have performed both longitudinal and transverse magnetotransport measurements on $MoTe_2$ flakes at 300mK as a function of thickness. Not only do we observe lower MR in thin samples, fittings to a two-band model surprisingly show a decrease in both the absolute and relative carrier concentrations as well as their mobilities. By modeling the different effects separately, we conclude that the MR is more sensitive to changes in carrier mobility, and that, in principle, relatively large MR values can be achieved with a moderate degree of charge imbalance.

3.2 Measurement and Analysis

3.2.1 Device Characterization

We performed AFM measurements to conclusively determine the thickness of eight $MoTe_2$ samples to be 7nm, 8nm, 10nm, 16nm, 20nm, 25nm, 50nm and 180nm. We measured temperature dependent resistivity for three representative $MoTe_2$ samples of different thicknesses (7, 50, and 180nm), results shown in Fig 3.2b. The traces are normalized to the resistivity at 280K and offset for clarity. All show metallic characteristics in contrast with an earlier report on unprotected thin flakes, which observes insulating behavior for thicknesses below ∼10nm [37].

A signature of temperature dependent T' to T_d phase transition is the observation of hysteresis loop at ∼250K, which gradually disappears for decreasing thickness as a single T_d phase is stabilized in thin flakes for the entire temperature range [47]. Below ∼10K, the resistivity saturates to a temperature-insensitive, residual value. In the inset, we have explicitly plotted the residual resistivity for all of the samples measured in this work (eight in total) at 300mK. While there is variation between samples, we observe no direct trend with flake thickness. Furthermore, the average residual resistivity $1.8\times10^{-5}\Omega$-cm (marked by dashed line) is comparable to that of the bulk crystal ($\sim10^{-5}\Omega$-cm) [11], indicating that our flakes have not degraded during the preparation process.

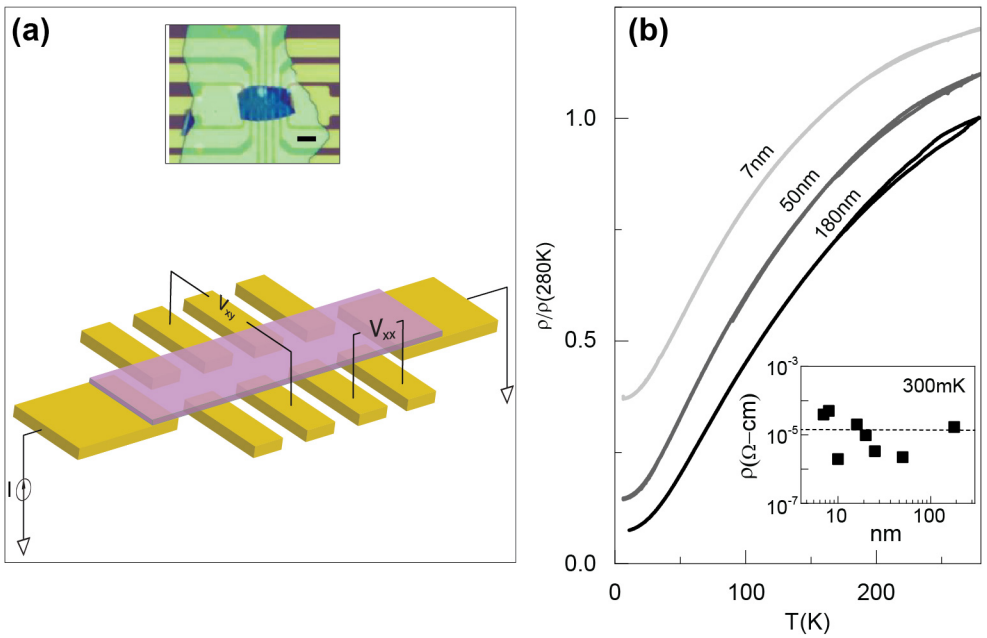

Figure 3.2: **Measurement Schematic and temperature induced phase transition.** **(a)** Device geometry and optical image of a representative device. $MoTe_2$ is covered with thin hBN to prevent oxidation. Scale bar is 10μm. **(b)** Main panel: normalized resistivity as a function of temperature for three $MoTe_2$ flakes of different thicknesses. An offset was applied to the upper traces for clarity. Metallic behavior is observed down to 4K for all samples. Inset: residual resistivity of all samples measured at 300mK. The dashed line marks the average resistivity.

3.2.2 Analysis based on two band model

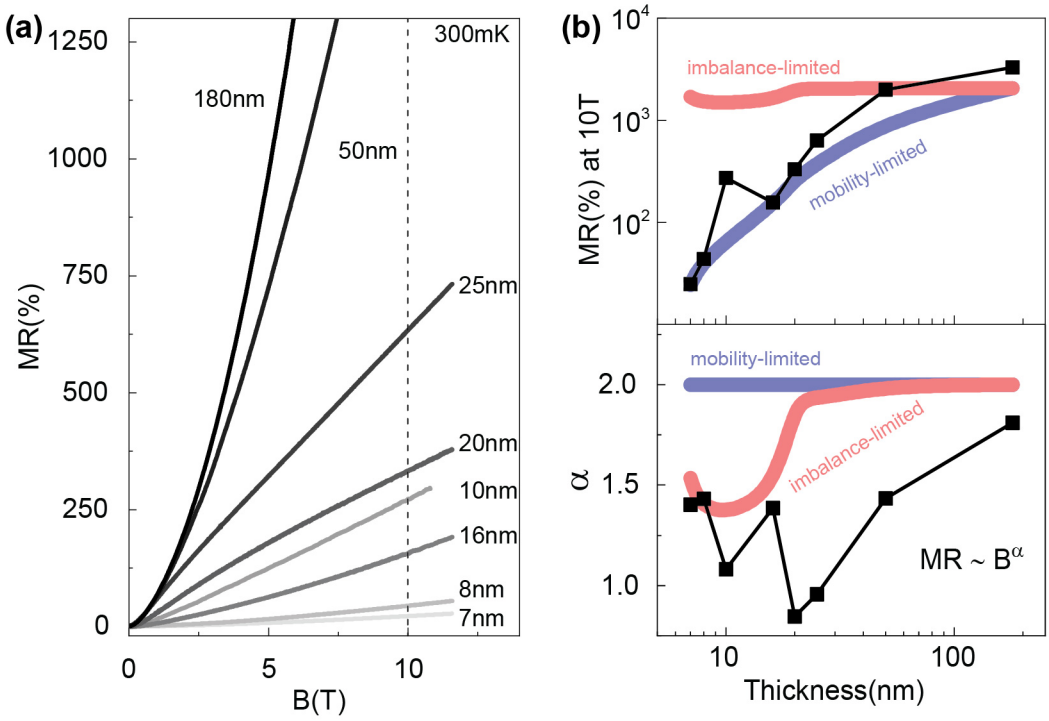

Figure 3.3: (a) Percent magnetoresistance as a function of perpendicular magnetic field. MR decreases with decreasing thickness. (b) The MR measured at 10T for the different samples. (c) Exponent α of power law fit to the field dependence. Magnetoresistance is sub-quadratic as the thickness is reduced. The effects of charge imbalance and mobility decrease on MR and α are modeled separately and plotted in red and blue, respectively.

We collected magnetoresistance data for both longitudinal and transverse resistance. The MR data display a strong thickness dependent behavior. In Fig. 3.3, we plot MR(%) = $\frac{\rho(B)-\rho(0)}{\rho(0)} \times 100$, for the eight samples at 300mK and field applied along the c-axis. While the MR is always positive and unsaturating, we observe a clear and systematic suppression with reduced thickness. In the top panel of Fig. 3.3, we explicitly plot the thickness-dependent MR measured at 10T. The value is ∼3000% in the 180nm flake, which is comparable to that measured in the bulk crystal [11], and decreases by two orders of magnitude in the

thinnest samples. Although the full Fermi surface of γ-$MoTe_2$ is complex and made up of multiple electron and hole pockets, the magnetotransport behavior may be understood from a simplified two-band model, where we assume that conduction takes place via one electron and one hole band only. Here, the field dependence of longitudinal and transverse resistivity obeys, respectively [9]:

$$\rho_{xx}(B) = \frac{(n\mu_n + p\mu_p) + (n\mu_p + p\mu_n)\mu_n\mu_p B^2}{e[(n\mu_n + p\mu_p)^2 + (p-n)^2\mu_n^2\mu_p^2 B^2]}$$
$$\rho_{yx}(B) = \frac{(p\mu_p^2 - n\mu_n^2)B + (p-n)\mu_p^2\mu_n^2 B^3}{e[(n\mu_n + p\mu_p)^2 + (p-n)^2\mu_n^2\mu_p^2 B^2]} \tag{3.9}$$

where n(p) and $\mu_n(\mu_p)$ refer to the electron (hole) concentration and mobility, respectively. If n=p, the first equation simplifies to MR=$\mu_n\mu_p B^2$, thus yielding unsaturating MR with a quadratic field dependence, as observed in bulk crystals [37, 11, 42]. The suppression of MR we observe in thin samples then suggests either (1) an imbalance of electrons and holes or (2) a decrease in their carrier mobilities. In order to distinguish between these two scenarios, we have first extracted the field dependent exponent from our data (MR$\sim$B$^\alpha$) using a power law scaling, and the result is plotted in the bottom panel of Fig. 3.3b. α is closer to 2 for thicker samples, but decreases with decreasing thickness, suggesting that the field dependent term in the denominator of ρ_{xx} becomes more dominant, and thus n$\neq$p for thinner flakes (scenario 1). The red and blue curves show the result of modeling the two scenarios separately, which will be discussed below.

We would like to determine quantitatively the carrier concentrations and mobilities for the different thickness flakes. Unlike ρ_{yx}, however, ρ_{xx} is insensitive to the carrier type. We have therefore measured both longitudinal and transverse resistivities in order to determine the full resistivity tensor of our samples, and the field (anti-)symmetrized results are shown in Fig 3.4. We have performed a simultaneous fit of ρ_{xx} and ρ_{yx} using the two-band model equations above (dashed lines in Fig 3.4, and the extracted carrier concentrations and mobilities are shown in Fig. 3.4c, along with the relative carrier concentration n/p. First, we note that the fit for ρ_{xx} is consistently larger than the measured values at higher fields beyond 8T. The reason for this is that degree of carrier imbalance, p-n, allowed

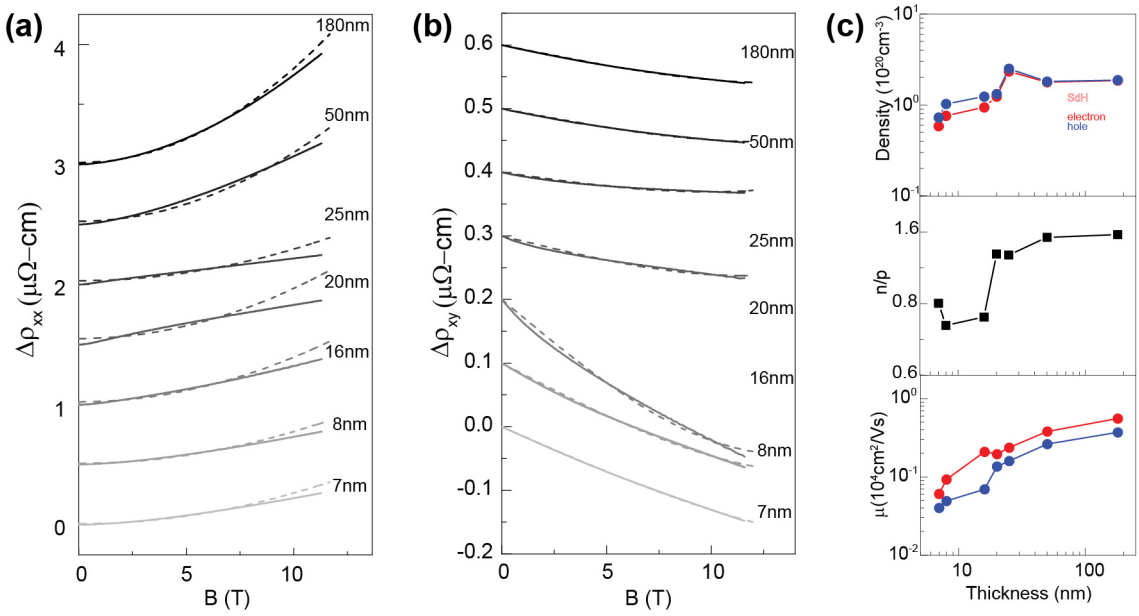

Figure 3.4: Summary of two band model fitting: Fitting of (a) longitudinal and (b)transverse resistivity over various thickness samples. (c) Plot of extracted carrier density and mobility.

for by ρ_{yx} is not sufficient to deviate ρ_{xx} strongly away from a B^2 dependence. Within the two-band model, we find that the density and mobility for both electrons and holes decrease slightly with reduced thickness. The ratio between electrons and holes, n/p, also decreases, indicating greater carrier imbalance. This behavior suggests that c-axis quantum confinement alone cannot account for the dimensionality-driven β to γ phase transition, as the electron pockets are mostly cylindrical [45, 49]. It is consistent, however, with the transition energetics calculated by Kim et al. [50], which reports overall shrinking of both surfaces accompanying the β to γ transition. The mechanism behind the thickness-driven effect therefore remains open question. Since both carrier imbalance and reduced mobility can suppress the MR, the two behaviors should be considered separately. In order to model this explicitly, we have taken the extracted carrier densities for the different thickness flakes and kept their mobilities constant and fixed to the values for the 180nm flake.

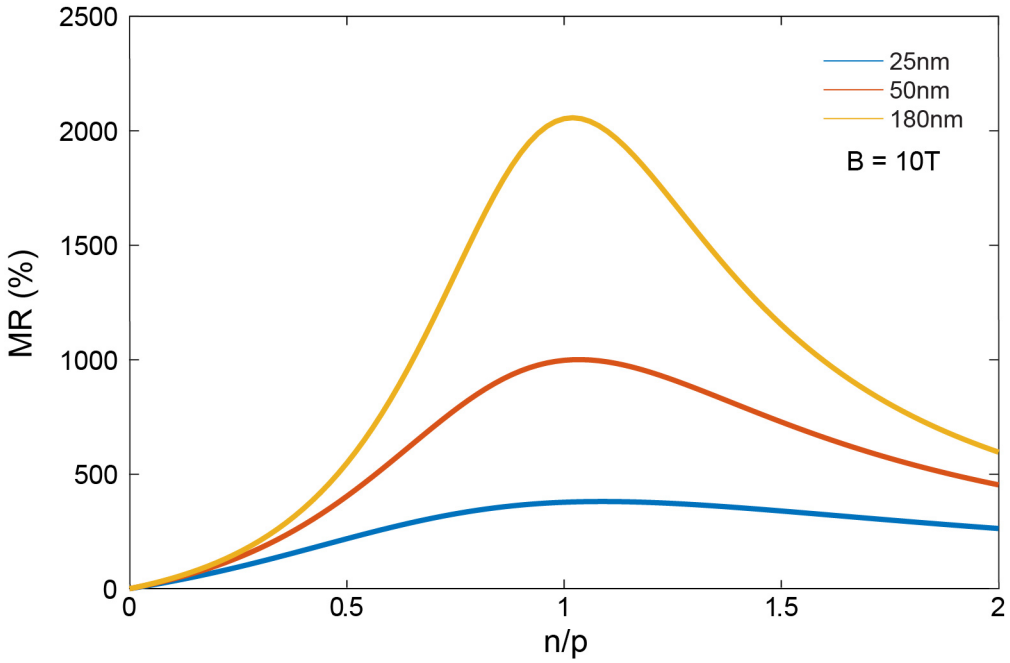

Figure 3.5: Magnetoresistance dependency on charge-imbalance over various thickness.

We then calculated the MR within the two-band model using these new parameters, and plotted the MR percentage at 10T as well as field-dependent exponent on top of the

original data in Fig. 3.3b in red ("imbalance-limited" curve). We similarly modeled the effect of reducing mobility only by fixing carrier densities fixed to the 180nm values. This is plotted in blue ("mobility-limited" curve). We observe that while sub-quadratic field dependence can be attributed to lack of charge compensation, the overall MR suppression is due to a reduction of carrier mobility. In principle, MR above 1000% may still be achieved in the thinnest samples, despite an imbalance ratio of n/p$\sim$0.8, as long as the mobility can be made large. Fig. 3.5 we have taken the extracted transport parameters from the two band model and plotted it by varying the n/p. It shows that the as thickness is reduced, magnetoresistance has less dependency on carrier compensation, therefore being less affected by a slight deviation from n/p$\sim$1.

3.3 Quantum Oscillations

Quantum oscillations are oscillations in the magnetization or resistance of a material with the external magnetic field. First observed in 1930 by de Haas and van Alpen as oscillations in magnetization in a single crystal Bismuth [51], analysis of these oscillations can help to map out the Fermi surface of a material under a strong magnetic field. Theoretical insight for these oscillations was given by Onsager in 1952 based on the Landau quantization of electron energy in a magnetic field. He proposed that the frequency(f) of the oscillations is proportional to the area of cross-section(A) of the Fermi surface, $f = \frac{\hbar}{2\pi e}A$, where proportionality constant is a universal constant, measuring quantum oscillation across different planes of a crystal can give the cross-section of full Fermi surface. In this section, we will look into the formation of quantized Landau levels as a solution to the Hamiltonian of a free electron under a strong magnetic field and consequences of these levels on the conductivity of a material.

3.3.1 Landau Levels

Magnetic field influences both the spin and the orbital motion of an electron. The impact on spin in metals gives rise to Pauli paramagnetism, while, on atomic orbitals leads to

quantization of electronic energy level under a sufficiently high magnetic field. Formation of Landau levels can be understood by solving the Schrodinger's equation of a system under a magnetic field.

$$\frac{\mathbf{p}^2}{2m^*}\psi = E\psi \tag{3.10}$$

where $\mathbf{p} = -i\hbar\nabla$ is the momentum operator. In the presence of a magnetic field $\mathbf{B} = (0, 0, B_z)$, momentum operator transforms as $\mathbf{p} = -i\hbar\nabla + e\mathbf{A}$, where $\mathbf{A}$ is magnetic vector potential, a useful[1] choice for the gauge potential could be $\mathbf{A} = (0, Bx, 0)$.

$$\left(\frac{p_x^2}{2m^*} + \frac{(p_y + eBx)^2}{2m^*} + \frac{p_z^2}{2m^*}\right)\psi = E\psi \tag{3.11}$$

By introducing $x_0 = -\hbar k_y/eB$ and cyclotron frequency $\omega_c = \frac{eB}{m^*}$, we have

$$\left[\left(\frac{\mathbf{p}_x^2}{2m^*} + \frac{1}{2}m^*\omega_c^2(x - x_0)^2\right) + \frac{\hbar^2 k_z^2}{2m^*}\right]\psi = E\psi \tag{3.12}$$

The above equation is a combination of Hamiltonian for one-dimensional harmonic oscillator along x-direction and free-electron in z-direction the corresponding energy eigenvalues will be:

$$E = (l + \frac{1}{2})\hbar\omega_c + \frac{\hbar^2 k_z^2}{2m^*} \tag{3.13}$$

where, l is an integer. The energy eigenfunction are a product of plane waves in the y and z direction, and a one dimensional harmonic oscillator wave function in the x direction. The application of a magnetic field causes the electrons to form Landau level with each level by quantum number l.

Interesting oscillatory changes in properties with magnetic field occur when Landau levels break through the Fermi surface as magnetic field is increased. Properties change because the density of states at the Fermi energy oscillate as a function of magnetic field. This effect is maximized when a Landau tube crosses an extremal cross-section of the Fermi surface. The oscillations in magnetization are known as de Haas-van Alphen effect.

[1] Any value for gauge potential is valid for which $B = \nabla \times A$ will not change, $A = (-B_y, 0, 0)$ would give the same value for B and energy eigen value but different eigen function.

The analogous effect on the electrical resistance is known as Shubnikov-de Haas effect. Both effects give rise to oscillations in properties as a function of 1/B. The period of these oscillations gives the area A_{ext} of the maximal and minimal cross-sectional area of the Fermi surface normal to the magnetic field.

3.3.2 Shubnikov-de Haas Effect

When magnetic field is applied to a system it forces moving electrons of the bulk to confine in a circular motion. For $B = B_z$, k_x and k_y states are restricted to circles, while k_z state remains unaffected. Increasing value of B_z causes Landau cylinders to move through the Fermi surface resulting into oscillations. When there are more than one region of the Fermi surface parallel to the Landau cylinders, it gives a beating pattern. Fourier transform of this beating pattern can give the different frequency components, and the amplitudes of the oscillations. The period of these oscillations the corresponding cross- sections is given by

$$\Delta\left(\frac{1}{B}\right) = \frac{2\pi e}{\hbar A_{ext}} \tag{3.14}$$

From equation 3.13, energy gap between two Landau levels is $\hbar\omega_c \propto B$. Therefore, increasing the magnetic field increases the gap between the levels. The energy of Landau levels with respect to the Fermi energy decides the impact of Landau level formation. If the highest Landau level is far from the Fermi energy, then no states are available for scattering, and the Shubnikov-de Haas resistivity goes to zero. Upon increasing the magnetic field, the highest Landau-level gets near the Fermi-energy, causing scattering of the bulk states. This scattering results in the peak of the Shubnikov-de Haas oscillations.

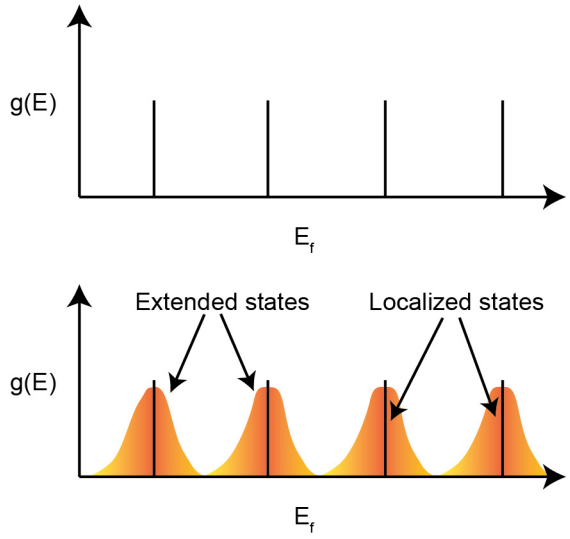

Figure 3.6: Landau level in a clean(top) and in a disordered(bottom) sample.

3.3.3 Damping in Oscillations

Temperature Effect

At a finite temperature the probability distribution of electron energy can be given by the Fermi distribution function:

$$f(E) = \frac{1}{1 + \exp(\frac{E-\mu}{k_B T})} \tag{3.15}$$

Thermally excited electrons can have energy levels outside of the Fermi surface. Shoenberg [52] suggested that this can be seen as a distribution of hypothetical metals with their Fermi energies distributed around E_F, and all being at T=0. The spread of Fermi surface area will lead smearing in the phase resulting into damping in oscillation amplitude as shown in Fig. 3.6. A quantitative description of magnetic oscillations was given by Lifshitz and Kosevich in 1954. The first harmonic l=1 of the LK formula for two dimensional electron gas at temperature T is:

$$A_1 \sim \frac{T}{2\sinh(\frac{2\pi^2 T m^*}{\hbar e B})} \tag{3.16}$$

By fitting this formula to the measured amplitude, the effective mass m^* can be extracted to calculate the mobility μ and carrier density.

$$m^* = \frac{\hbar\sqrt{\pi n}}{v_F^*} = \frac{\mu}{v_F^{*2}} \tag{3.17}$$

3.4 SdH oscillations in $MoTe_2$

At high magnetic fields the details of scattering processes become less important allowing to study the Fermi surface more closely. SdH oscillations have previously been observed in high-quality $MoTe_2$ crystals, which allows for an independent measurement of the Fermi surface [37, 49, 43]. We have observed oscillations for the 10nm, 20nm, and 180nm flakes at 300mK. Their background resistivities were subtracted and the results are plotted as a function of 1/B in the insets of Fig. 3.7. The samples show a beating pattern, thus indicating the presence of more than one frequency. We have taken the fast Fourier transform (FFT) of the SdH oscillations and the result is shown in the main panel of Fig. 3.7a. We observe two clear peaks for all samples and possibly three for the 20nm flake, which show oscillations starting at lower field. For the 180nm flake, the peak positions (202T and 266T) are similar to what has been observed in the bulk crystal [49], and correspond to carrier densities of 0.70×1020 cm^{-3} and 0.93×1020 cm^{-3}, respectively, via the Onsager relation. Density functional calculations indicate these oscillation frequencies are associated with electron pockets [49], while the hole pocket frequencies either exceed 1000T or fall below 100T. For the thinner flakes, these two peaks are systematically shifted to lower fields, and thus densities. In Fig. 3.7c, we have plotted the sum of the densities extracted from the positions of the two prominent peaks (open red circles) in order to compare with the concentrations obtained from the two-band model. The thickness dependence is qualitatively consistent, although the electron density estimated from classical magnetotransport is lower in thinner samples. We have further performed the same measurement on the 20nm flake, which shows the most prominent oscillations, as a function of temperature (see Fig. 3.7b). By fitting the peak amplitudes to the Liftshitz-Kosevich (LK) formula, we obtained an estimate of the effective masses (∼1.0-1.2m_0), which are slightly larger than those measured for the bulk crystal (∼0.8m_0).

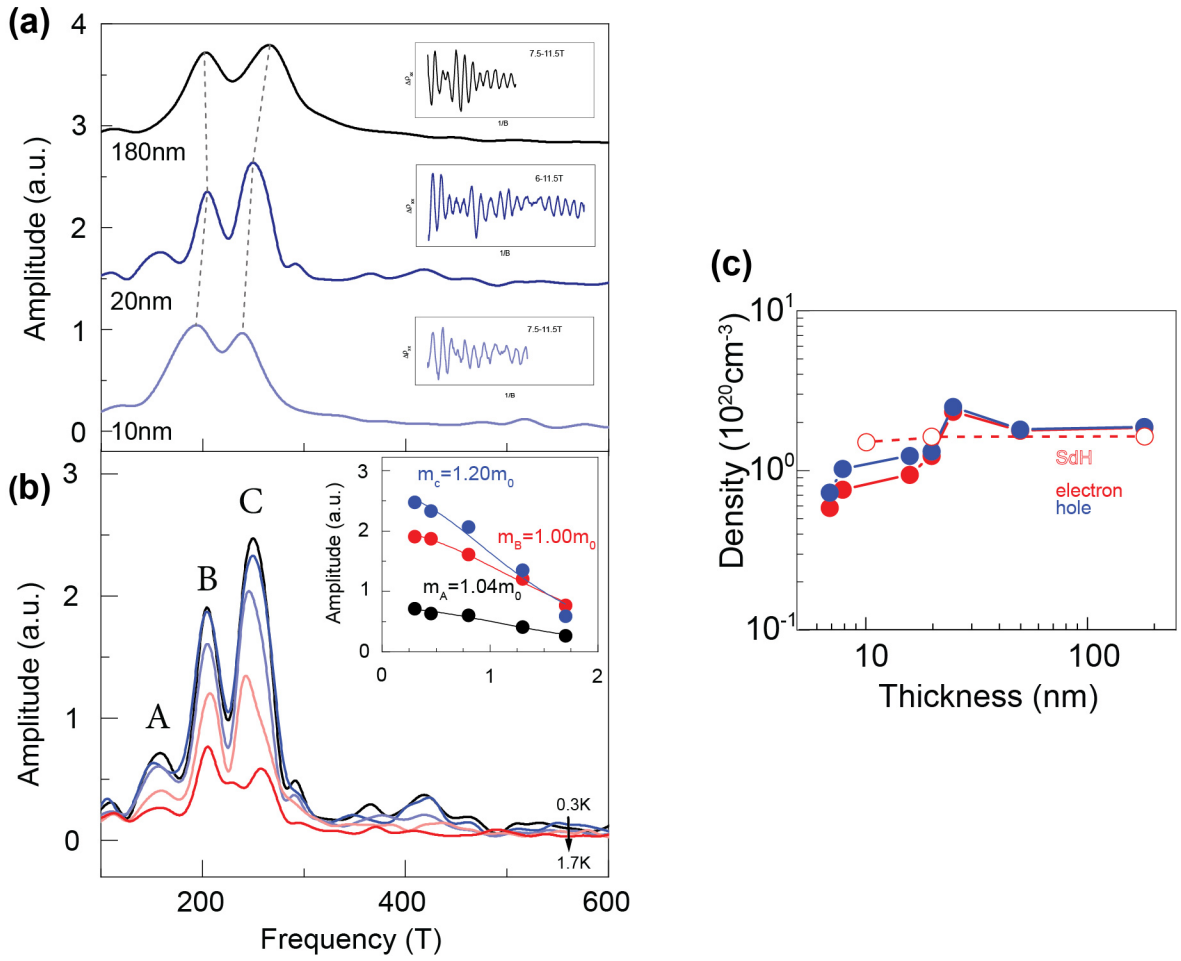

Figure 3.7: **SdH oscillations in the longitudinal resistivity of $MoTe_2$.** **(a)** Inset: SdH oscillations observed after subtracting the polynomial background for each sample. Their corresponding FFT is shown in the main panel. The dashed lines are guides to the eye showing decreasing frequencies with decreasing sample thickness. **(b)** Main panel: The FFT of the SdH oscillations for the 20-nm sample measured at 0.3, 0.45, 0.8, 1.3, and 1.7 K. Inset: The amplitude of the FFT peaks as a function of temperature fit to the LK formula to extract the effective masses. **(c)** The carrier densities for different thickness samples extracted from the simultaneous fit of ρ_{xx} and ρ_{yx} using the two-band model, compared with the values extracted from the SdH oscillations(open circle).

3.5 Conclusion

We used magnetotransport measurements to study the thickness evolution of electronic structure in γ-$MoTe_2$ at low temperature. We observed a decrease in both electron and hole densities as well as mobilities in thin flakes. The decrease in electron and hole density possibly stabilizes the γ phase in thin flakes at room temperature, while the decreased mobility greatly suppresses the XMR effect. It may be possible to still achieve very large MR values without near-perfect charge compensation, this can potentially interesting consequences for the tailoring of XMR in future materials.

Chapter 4

Non-linear Transport in $MoTe_2$

In the previous chapter, we employed thickness induced structural phase transition of a transition metal dichalcogenide (TMDC) material $MoTe_2$ to study carrier mobility, carrier density imbalance and their impact on large magnetoresistance. In this chapter, we will look into the symmetry properties exhibited by TMDC class materials $MoTe_2$ and WTe_2, and symmetry dependent non-linear transport properties.

Underlying symmetry of a crystal decides its response to perturbations of electric and magnetic field, this accounts for observation of helicity dependent photocurrent response [53, 54], and non-linear transport properties [55, 56, 57, 58, 59, 60]. An interesting consequence of inversion symmetry breaking under an electric field is the observation of non-linear Hall like effects in three-dimensional non-centrosymmetric crystals, topological crystalline insulators, two-dimensional TMDCs, and polar materials [61]. This non-linear Hall effects can be explained based on the idea of anomalous Hall effect (AHE), which until recently was only explored in the systems with broken time reversal symmetry. AHE originates from both the intrinsic picture of Berry phase dependent anomalous velocity and extrinsic factors resulting from spin-orbit interaction of electron with crystal lattice and impurities. Intrinsic picture which is most studied and well understood at this point has been driven a lot interesting work. Extrinsic mechanism which depends on a details of scattering process [62] significantly impacts the overall strength of the Hall effect [63, 64, 65], and becomes largely important when application of Hall effect in real devices is concerned.

In this chapter, we will discuss the findings of non-linear anomalous Hall effect (NLAHE) in non-centrosymmetric TMDCs $MoTe_2$ and WTe_2. We will start with a brief discussion on anomalous Hall effect explaining the mechanisms involved in it. We then proceed to look into the symmetry constraints for the $MoTe_2$ and WTe_2 and then design measurements accordingly. We perform both first and second harmonic measurements along in-plane and out-of-plane direction to measure longitudinal and transverse conductivity. To parse different contributions to the NLAHE, we will be introducing a scaling law with respect to the longitudinal conductivity, and discussing the mechanism responsible for this effect. To quantify the strength of the observed effect, we give a measure for the Hall ratio, and finally to put this work in context with the available literature we present a map of Hall conductivity across various AHE experiments.

4.1 Anomalous Hall Effect

In ferromagnetic conductors, passage of charge current can generate an electric field in the transverse direction even without the application of an external magnetic field. This "anomalous" Hall effect (AHE) requires broken time reversal symmetry and originates both from topological aspects of the material's band structure and electron scattering coupled to the spin-orbit interaction.

In the following section, we will discuss these different mechanisms, and their validity in different conductivity regimes. Conventionally, classification for different contributions is based on dependence of anomalous Hall conductivity (σ_{AHE}) on Bloch state transport time (τ). Experimentally, it is achieved by plotting σ_{xy} vs $\sigma_{xx} \propto \tau$, where τ can be varied by controlling the disorder or temperature. The two leading contributions to AHE are τ^0 and τ^1, since disorder are treated perturbatively they correspond to higher order term τ^1. Hall resistivity can be written as $\rho_{xy} = \frac{\sigma_{xy}}{\sigma_{xx}^2+\sigma_{xy}^2}$, varies as $\rho_{xy} \sim \rho_{xx}^2$ and $\rho_{xy} \sim \rho_{xx}$, for intrinsic and extrinsic mechanisms, respectively.

4.1.1 Intrinsic Mechanism

In 1954, Karplus and Luttinger [66] proposed that spin-orbit interactions of polarized conduction electrons can explain the observed large magnitude and temperature dependence of anomalous Hall effect in Ferromagnetic materials. They explained that in the presence of an external electric field electrons faces a transverse force but left and right symmetry is maintained, however, in systems where time reversal symmetry is broken an asymmetry is developed, giving an additional contribution to the electron velocity. This velocity when summed over all occupied bands contributes to anomalous conductivity. After the introduction of Berry phase [67] in 1984, a connection between anomalous velocity of Bloch electrons and Berry phase was established by Change et al. [68] and Sundaram et. al. [69], that anomalous conductivity can be understood as the sum of Berry curvature over the occupied bands.

To understand the microscopic picture we can look into the velocity of electron wave packet in a crystal lattice in the presence of magnetic field. The group velocity can be written as:

$$\frac{\partial \langle \vec{r} \rangle}{\partial t} = \frac{\partial \varepsilon}{\hbar \partial k} + \frac{e}{\hbar} E \times \Omega(k) \tag{4.1}$$

The quantum origin comes from the contribution of Berry curvature ($\Omega(k)$) which is non-zero in systems with either broken time reversal or broken inversion symmetry. The anomalous Hall conductivity of a system can be written as: $\sigma_{AHE} = \int d^2k f(k)\Omega(k)$, where f(k) is the Fermi distribution function. In time reversal symmetric systems, Berry curvature transforms as an odd function, $\Omega(k) = -\Omega(-k)$, which under equilibrium Fermi distribution will give a zero Hall conductivity. However, under a non-equilibrium Fermi distribution this can lead to a finite Hall conductivity.

As this contribution purely depends on the band structure of the crystal and doesn't account for the phonon and impurity related scattering it is called an intrinsic mechanism. It is the most studied contribution which can be derived from the first principle contribution of the electronic band structure and found to be a dominant factor in the system with high spin-orbit interaction. Although it can explain the anomalous velocity of the electron in the absence of magnetic field for a perfect crystal under realistic conditions the imperfections

of the crystal need to be considered. Their contribution towards the asymmetric scattering of electrons in a crystal can be explained by extrinsic mechanism below.

4.1.2 Extrinsic Mechanism

A semiclassical explanation for extrinsic contributions to AHE was given by Smit[70, 71] and Berger[72], which talks about the effect of disorder scattering in imperfect crystals. Both asymmetric and symmetric scattering can be attributed to the spin orbit coupling of the electron with the impurity potential. The extrinsic contribution was calculated from the expectation value of the position operator after the collision with the impurity as depicted in the Fig. 4.1. First, the center of wave packet shifts in the direction transverse to the velocity of the electron after scattering giving side-jump contribution. Second, the expectation value continuously deviates in time from the initial path of the wave packet giving skew-scattering contribution. This scattering is spin-dependent with opposite spins scattering in opposite directions. Considering the electron scattering from an impurity. The Hamiltonian for this problem can be written as following:

$$H = H_0 + H_{so}$$
$$H_0 = p^2/2m + U(r)$$
$$H_{so} = \frac{\hbar^2}{2m^2c^2}\frac{1}{r}\frac{dV}{dr}(l \cdot S)$$

Here, U(r) is the impurity potential, $l = (r \times p)/\hbar$ and S are the orbital momentum and the spin of the electron, respectively.

Skew-scattering

In the linear transport regime, scattering of electrons from impurities or phonons is balanced by the applied electric field E giving a steady state current. Taking this into account, Smit argued that under steady state the anomalous velocity proportional to $\dot{k}$ will vanish, and the temperature variation shows the dependence on the electrical resistivity of the material [70, 71]. Spin orbit coupled electrons upon scattering from the impurity gets deflected

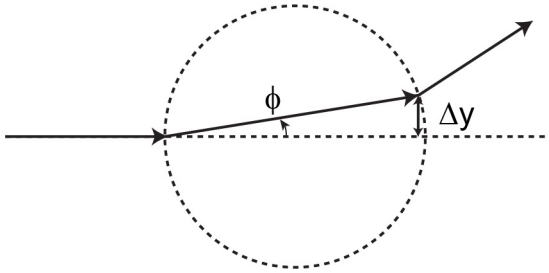

Figure 4.1: Scattering of polarized electron from impurity potential. ϕ is the skew-scattering contribution and Δy is side-jump contribution. Adopted from [2].

in a direction perpendicular to the momentum k and magnetization M, for a perfect crystal this scattering will have left and right symmetry, giving no contribution to the overall Hall effect. However, for an imperfect crystal this produces an asymmetric scattering causing a net transverse velocity. The transition probability associated with collision is given by equation 4.2 involving the chiral term coming due to spin-orbit coupling in both perfect crystal and disorder Hamiltonian.

$$W_{n\to n'} = \frac{2\pi}{\hbar}|\langle n|V|n'\rangle|^2\delta(E_n - E_{n'}) \tag{4.2}$$

Microscopic detailed balance which decomposes the kinetics of a system in elementary processes states that at equilibrium each elementary process is reversible in nature. However, it fails in the calculation of Hall conductivity which involves higher order impurity potential terms. Skew-scattering is give by the asymmetric part of the transition probability

$$W^A_{kk'} = -\tau_A^{-1} k \times k' \cdot M_s \tag{4.3}$$

This asymmetry is indicative of different scattering probability for W($k \to k'$) and W($k' \to k$). Including this contribution in the linearized Boltzmann equation gives the transverse velocity component.

Side-jump

The semiclassical picture of side-jump mechanism proposed by Berger [72] considers the scattering of a Gaussian wave packet from a spherical impurity with spin orbit interaction,

resulting into a transverse displacement with respect to the wave vector k. Assuming a spherical potential well of radius R of the following form,

$$V(r) = \begin{cases} 0 & r > R \\ \frac{\hbar^2}{2m}(k^2 - k_l^2) & r < R \end{cases} \tag{4.4}$$

For a finite spin-orbit interaction term $H_{so} = (1/2m^2c^2)(r^{-1}\partial V/\partial r)S_zL_z$ with $S_z(L_z)$ as z-component of spin(orbital) angular momentum. The corresponding transverse displacement Δy for an incident wave-packet with wave vector k is

$$\Delta y = \frac{1}{6}k\lambda_c^2 \tag{4.5}$$

where $\lambda_c = \hbar/mc$ is the Compton wavelength. For $k \sim k_F \sim 10^{10}m^{-1}$ (typical metals), $\Delta y \sim 3 \times 10^{-16}$m is too small to be measured. However, in solids, the effective spin-orbit interaction is enhanced by band-structure effects by a factor of

$$\frac{2m^2c^2}{m^*\hbar}\tau_q \sim 3.4 \times 10^4 \tag{4.6}$$

with this enhancement, the transverse displacement is $\Delta y \sim 0.8 \times 10^{-11}$m.

4.2 Non-linear anomalous Hall effect (NLAHE)

Although it was theoretically established that anomalous Hall effect can result from a finite Berry curvature in the system which retains time reversal symmetry and have broken inversion symmetry [68, 69]. It wasn't until Moore and Orenstein's work relating DC photocurrent observed in a realistic two dimensional system with Berry phase induced due to quantum confinement that an experimental connection was achieved [53]. They discussed the results in regard with the optically inactive media showing helicity dependent response [73, 74], as a Berry-phase effect driven by inversion symmetry breaking.

A more generalized version of this theory was given by Sodemann and Liang Fu [61] suggesting that Hall-like currents can be observed as the second-order response to the external electric fields in time-reversal invariant systems with broken inversion symmetry as

both DC and second harmonic response to the driving frequency. This non-linear Hall effect arise from the Berry curvature dipole (BCD) in the momentum space, generating a net anomalous velocity when system is in non-equilibrium (current carrying state). The non-linear Hall coefficient is a rank two pseudo-tensor whose form is determined by the point group symmetry. Inversion-symmetry breaking may cause segregating the positive and negative Berry curvature in different regions in momentum space causing a net dipole moment. Nonlinear effect can be observed upon applying an electric field along the direction of this dipole moment. Since then there has been many theoretical [75, 76, 77] and experimental [56, 78, 57, 59] reports trying to elucidate the underlying mechanism.

In non-centrosymmetric materials retaining time reversal symmetry, it is possible to realize a "nonlinear AHE" (NLAHE), whereby the current induces an effective magnetization in the sample and establishes a transverse electric field that increases quadratically with applied electric field [61, 75, 79, 80, 20]. Experimentally, an AC voltage of frequency ω is applied across the sample and a voltage of either frequency 2ω or 0 (DC) is detected in the transverse direction. Such an effect was first demonstrated in two-dimensional (2D) WTe_2 within the plane of the layers [56, 55]. They tune the Fermi level by gating the device, and show that at a charge neutrality point a large non-linear response is observed. They attribute it to the intrinsic contribution coming from the dipole moment of Berry curvature arising from the layer-polarized Dirac fermions in bilayer WTe_2. Another work on few layer WTe_2 showed crystalline axis and temperature dependence of the non-linear Hall effect [78]. They attribute the effect to both intrinsic Berry curvature dipole mechanism and extrinsic spin-dependent scatterings. A quantitative result on the non-linear Hall effects arising from the Berry curvature dipole moment in the non-centrosymmetric Weyl semimetals was reported by [79]. They discuss the type I, TaAs, and type II $MoTe_2$ and WTe_2, Weyl semimetal systems concluding that the tilted Weyl cone of Type-II semimetals result in larger BCD. Berry curvature dipole is given by

$$D_{ab} = \int_k f_0 \frac{\partial \Omega_b}{\partial k_a} \tag{4.7}$$

The left side of 4.2 shows the crystal structure of T_d-$MoTe_2$. The a and b axes lie within the plane of the layers, while the c-axis points out-of-plane. In addition to a mirror plane that is normal to the a-axis, there is a glide plane that is normal to the b-axis and a two-

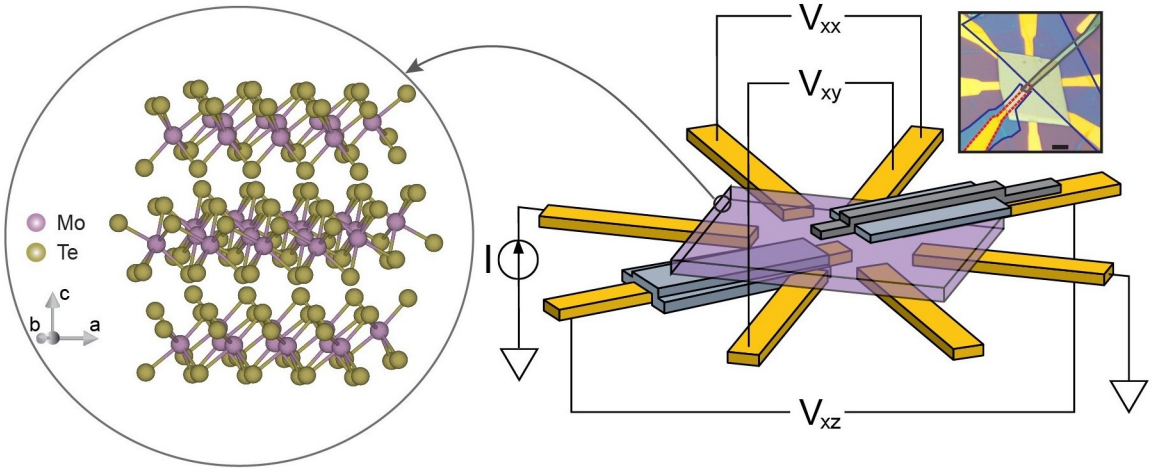

Figure 4.2: **NLAHE measurement schematic.** Main panel: crystal structure of $MoTe_2$ in the T_d phase and device geometry. Purple, blue, and gray flakes represent $MoTe_2$, h-BN, and graphene, respectively. Inset shows optical image of 70-nm-thick device. h-BN blocking layers, graphene, and the bottom vertical contact are outlined in blue, gray, and red, respectively. Scale bar is 5μm.

fold screw axis along the c-axis, putting the bulk crystal in the non-centrosymmetric space group $Pmn2_1$ [81]. The corresponding point group mm2 has the nonlinear susceptibility tensor, $\begin{bmatrix} 0 & 0 & 0 & 0 & d_{15} & 0 \\ 0 & 0 & 0 & d_{24} & 0 & 0 \\ d_{31} & d_{32} & d_{33} & 0 & 0 & 0 \end{bmatrix}$. For the application of an in-plane electric field of frequency ω: $[E_b^\omega, E_a^\omega, 0]$, a vertical Hall current at frequency 2ω: $j_c^{2\omega} = d_{31}(E_b^\omega)^2 + d_{32}(E_a^\omega)^2$, develops along the c-axis, while nonlinear currents in-plane strictly vanish: $j_b^{2\omega} = j_a^{2\omega} = 0$. In contrast, since the glide plane and screw axis symmetries are broken for the surface layers, ultrathin samples understood to be in space group Pm [82], with allowed nonlinear currents both in-plane and out-of-plane.

To design a measurement for understanding mechanism behind NLAHE, we have gathered following information. For TMDC materials $MoTe_2$ and WTe_2 the allowed direction for NLAHE is along the c-axis. Since there could potentially be conductivity dependent skew scattering contribution, NLAHE should be have a crystalline axis dependency for an anisotropic crystal. Therefore, we need to fabricate a device which can incorporate requirements of current injection from both planer axis(a & b), in-plane Hall measurement, four-terminal longitudinal voltage measurement and a pure c-axis contact for eliminating any mixing with in-plane components.

4.3 Experimental Methods

4.3.1 Sample Fabrication

To measure c-axis NLAHE, we have fabricated samples with vertical as well as in-plane contacts. In particular, our devices consist of underlying gold electrodes with $MoTe_2$ crystals of various thicknesses transferred on top. To maintain consistency, all $MoTe_2$ flakes were exfoliated from a single piece of bulk crystal grown by the flux method. Few-layer graphene was used as a vertical top electrode with insulating hexagonal boron nitride (h-BN) blocking all but the tip of the vertical contacts to prevent mixing with in-plane currents and fields. In order to protect the sample from degradation, the entire transfer process was performed within a nitrogen-filled glovebox. A device schematic is shown (without the

top h-BN layer for clarity) in Fig. 4.2, and an optical image of a representative device is shown in the inset.

Since current applied along the a- and b-axis of the crystal generally give rise to different nonlinear Hall currents or fields as per the different elements of the susceptibility tensor d_{31} and d_{32}, we have controlled for the sample orientation by selecting $MoTe_2$ flakes that were rectangular in shape and aligning them with the circular electrode pattern. This allows for current injection along both the long and short directions of the flake in the same device, which in almost all cases correspond to the a- and b-axis, respectively. For either current I‖a or I‖b, our device geometry yields measurement of the following linear and nonlinear voltages: in-plane longitudinal (V_{xx}), in-plane Hall (V_{xy}), and out-of-plane Hall (V_{xz}).

4.3.2 Measurement Set Up

Transport Measurements

Both the magnetotransport and NLAHE measurements were primarily carried out in a pumped Helium-4 cryostat (Cryo Industries of America) with a base temperature of 1.4K. The latter was further cross-checked in a Montana Instruments Cryostation with base temperature of 5K. For the second harmonic NLAHE measurements, an AC current with frequency between 17 to 277Hz was passed along either the a- or b-axis of the $MoTe_2$ crystal, and V_{xx}, V_{xy}, and V_{xz} voltages were measured at both the first harmonic (X channel) and second harmonic (Y channel) frequencies using an SR830 lock-in amplifier. A Keithley 2450 source measure unit was further used to measure the DC voltage response of the NLAHE.

Optical Second Harmonic Generation Measurements

Rotational anisotropy SHG measurements were taken in a normal incidence geometry using a pulsed laser with a pulse duration of ∼325 fs, a repetition rate of 200 kHz, and an incoming fundamental wavelength of 800 nm. The $MoTe_2$ samples were held at 80K inside an optical cryostat. Using a single-photon sensitive detector, the intensity of the reflected SHG was

measured as a function of the angle between the incident polarization and the x-axis in the lab coordinate frame. The incident fundamental and the reflected SHG polarizations can be selected to be either parallel or crossed, forming two polarization channels for the SHG measurements.

4.4 Measurement & Analysis

This section includes measurement and results on device characterization using optical second Harmonic generation, and magnetoresistance measurement, low temperature second harmonic transport on both WTe_2 and $MoTe_2$.

4.4.1 Device Characterization

In order to confirm the crystal orientation, we first measured the longitudinal magnetoresistance, MR=[$V_{xx}(B_\perp)$-$V_{xx}(0)$]/$V_{xx}(0)$ for constant current, along the two current directions. Fig. 4.3a shows representative data from a 47-nm-thick device at 1.4K: I‖a (I‖b) exhibits quadratic (linear) magnetoresistance up to 12.5T, consistent with previous measurements on bulk crystals [10]. Overall, MR is large and non-saturating due to close electron-hole compensation combined with relatively high carrier mobilities [9, 37, 79]. In addition, we have performed optical second harmonic generation (SHG) measurements, which can also distinguish between the a- and b-axis of $MoTe_2$. Fig. 4.3b shows SHG intensity measured on the same sample at 80K with incident and scattered light polarization in parallel as a function of the polarization angle relative to the a-axis, at which a node can be seen, consistent with previous results [83]. Unlike the electrical second harmonic measurements we are to present, optical SHG is mostly sensitive to the symmetry properties of the surface layers, which allow for in-plane responses.

4.4.2 Non-linear Hall measurements

Fig. 4.4 shows representative NLAHE measurements taken on a 127-nm-thick sample at 2K. The upper two panels show V_{xz} measured at DC and second harmonic (2ω= 354Hz)

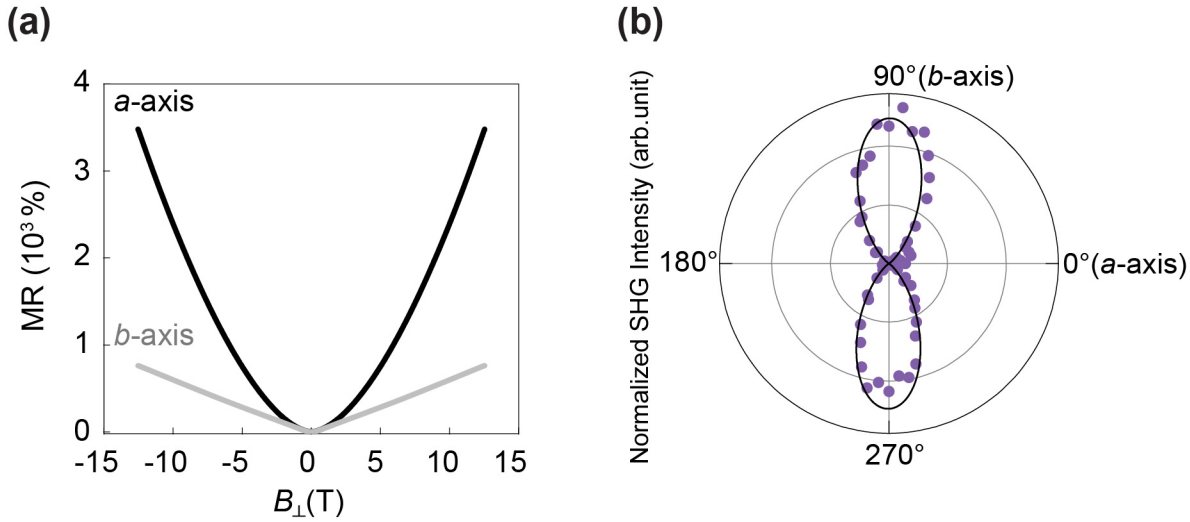

Figure 4.3: **NLAHE sample characterization.(a)** Symmetrized MR of 47-nm-thick device with current applied along the a and b crystal axes at 1.4K. I||a (I||b) exhibits quadratic (linear) MR. **(b)** Angle-dependent second harmonic generation measured on the same sample. Minimum (maximum) intensity occurs along the a-axis (b-axis).

frequencies as a function of the first harmonic (ω=177Hz) V_{xx}^2 for I||a and I||b. All four traces show linear behavior at low bias as expected for the NLAHE [78], although the slope is larger for current along the a-axis. At higher bias the curves become slightly sublinear, possibly due to sample heating. Furthermore, for each current direction, the DC and 2ω amplitudes are comparable for a given applied bias. In contrast, as shown in the lower two panels, relatively small second harmonic voltage is measured for V_{xx} or V_{xy} for comparable bias, consistent with the allowed symmetries discussed earlier for bulk-like crystals.

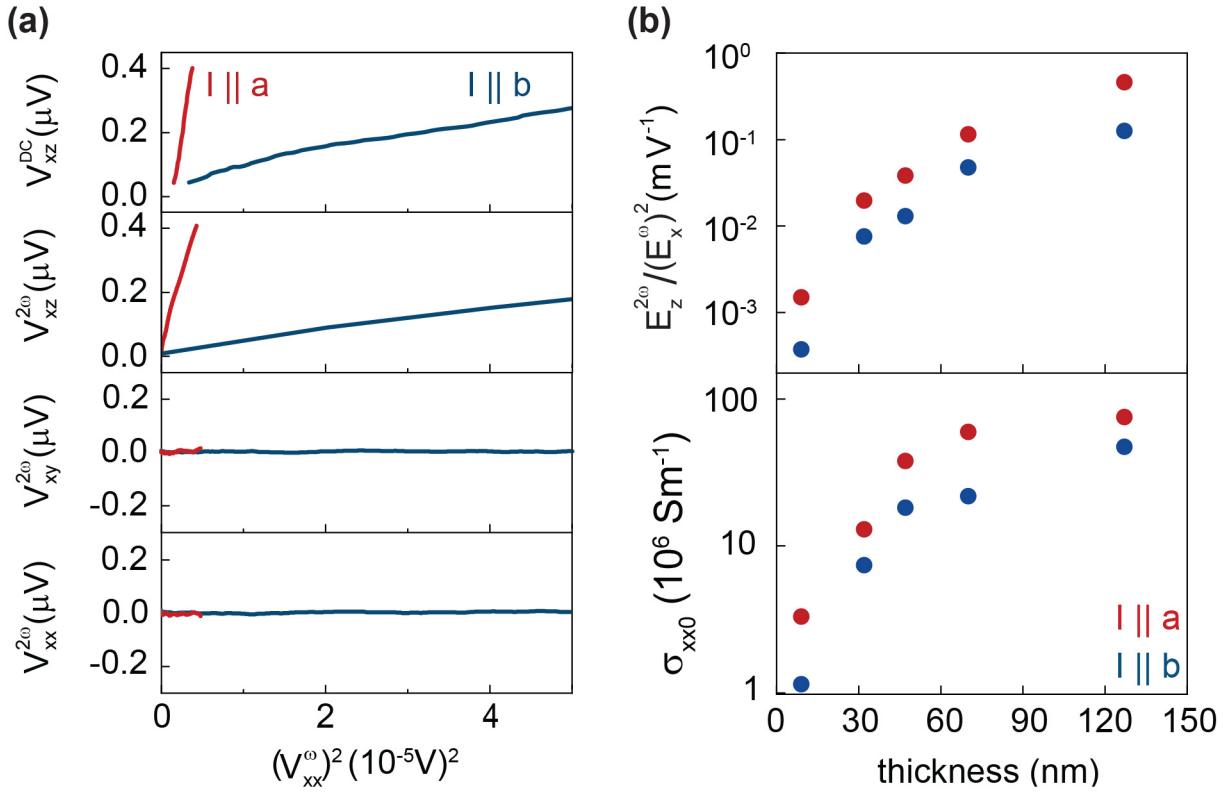

Figure 4.4: **Dependence of NLAHE on crystal axis and thickness.** **(a)** Upper panels: DC and second harmonic V_{xz} vs. first harmonic V_{xx}^2 for I||a and I||b in 127-nm-thick sample at 2K. Lower panels: analogous second harmonic measurements for in-plane response show significantly weaker signal under comparable bias. b, NLAHE strength $E_z^{2\omega}/(E_x^{\omega})^2$ and residual longitudinal conductivity σ_{xx0} vs. sample thickness for I||a and I||b. Both values are larger for greater thickness and I||a.

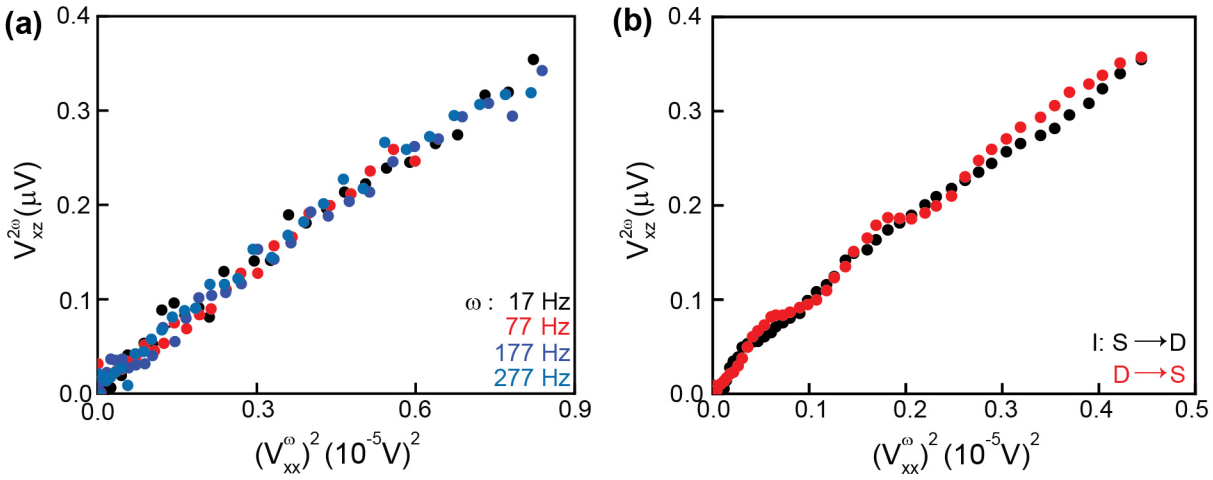

Figure 4.5: **Fidelity of NLAHE signal.** The c-axis NLAHE does not substantially change with **a** changing first harmonic frequency or **b** exchanging the current leads.

The Fig. 4.5 show that these results do not change when the frequency ω is changed over an order of magnitude or by exchanging the current leads, indicating that they stem from intrinsic properties of the sample.

For the remainder of this work, we will focus only on the second harmonic component of the c-axis NLAHE. The strength of this effect can be defined as the slope of the linearized plots presented at low bias. In order to understand and demonstrate the reproducibility of these results, we have performed similar measurements across five samples of different thicknesses down to the 2D limit: 127, 70, 47, 32, and 9nm. The NLAHE strength is shown as a function of sample thickness for both I‖a and I‖b in the upper panel of Fig. 4.4b. We have used electric field values, $E_z^{2\omega}/(E_x^{\omega})^2$, instead of voltage in order to account for the different dimensions of the samples. The local E_x^{ω} at the vertical contact area was obtained from finite element method simulations of each individual device. For every sample, the a-axis shows larger strength than the b-axis, while for both axes, the strength decreases substantially with decreasing thickness. In particular, for I‖a in the thickest (127nm) sample, $E_z^{2\omega}/(E_x^{\omega})^2 = 0.43\text{m/V}$.

The differences observed between the samples and two crystalline axes can be attributed to their differences in conductivity. In the lower panel of 4.4b, we have plotted the residual

longitudinal conductivity σ_{xx0} for each sample and axis, which shows a similar trend. This reflects the three-dimensional electronic character of $MoTe_2$-decreasing thickness increases surface scattering, which lowers the residual conductivity by over an order of magnitude in our thinnest sample, consistent with previous results from the previous chapter.

4.4.3 Scaling relation in NLAHE

Scaling relation between anomalous Hall resistivity and longitudinal resistivity has been central tool in parsing different contributions to the anomalous Hall effect. It is generally believed that AHE has three key components as discussed in section 4.1. $\sigma_{AH} = \sigma_{int} + \sigma_{sk} + \sigma_{sj}$ where σ_{int}, σ_{sk}, σ_{sj} are contributions from KL intrinsic effect, skew scattering and side-jump mechanism, respectively. A recent temperature dependent scaling was proposed by [62], where comprehensive scattering mechanisms were included.

$$\sigma_{AH} - \alpha_0 \sigma_{xx}^2/\sigma_0 = \beta(T) + \beta^{'}(T)\sigma_{xx}/\sigma_0 + \beta^{"}(T)(\sigma_{xx}/\sigma_0)^2 \tag{4.8}$$

where βs are temperature dependent coefficients arising from combinations of interaction between electron-impurity and electron-phonon scattering, α_0 is contribution from impurity skew-scattering. Fig. 4.6a, shows the temperature dependence of $E_z^{2\omega}/(E_x^{\omega})^2$ and conductivity measured for the 127-nm-thick sample-both decrease with increasing temperature. In the lower inset, we show the temperature-dependent longitudinal resistivity for I‖a in the same sample, which conversely decreases with decreasing temperature. Specifically, the resistivity scales linearly with temperature at higher temperatures, but begins to saturate in the crossover region roughly centered at T_L ∼18K.

Taken together, these results indicate that conductivity (or resistivity) may be the fundamental parameter upon which the NLAHE strength depends. To show this dependence explicitly, the main panel of Fig. 4.6b shows the log-log scale, $E_z^{2\omega}/(E_x^{\omega})^2$ for both axes of each sample versus temperature-dependent conductivity normalized to the residual conductivity, σ_{xx}/σ_{xx0}, and a general trend appears to emerge. Specifically, at lower conductivity (higher temperature) for a given sample and axis, $E_z^{2\omega}/(E_x^{\omega})^2$ scales closely with σ_{xx}^2 as

compared with the guide-to-eye in gray. Above (below) a certain conductivity (temperature), it increases at an even faster rate. To see this crossover point more clearly, we have extracted the local slope ν from the data in the main panel as a function of temperature (normalized to the T_L of each sample/axis, which ranges between 13-18K), yielding the relationship $E_z^{2\omega}/(E_x^{\omega})^2 \sim \sigma_{xx}^{\nu(T)}$. The inset of Fig. 4.6 shows ν(T) for all the different traces in the same color scheme as that used in the main panel. Above T_L, ν is near 2 for every trace, while it rises continuously below this temperature. We have also performed similar measurements on bulk-like WTe_2 (which shares the same crystal structure) as well as $MoTe_2$ Hall bar devices for I‖a, both of which show qualitatively similar behavior. This indicates that the strength and scaling of the c-axis NLAHE is not unique to $MoTe_2$ nor a result of the circular electrode geometry.

In order to understand the mechanism behind the NLAHE and the observed scaling with longitudinal conductivity, we turn to the theory behind the ordinary AHE, as it is understood that the NLAHE strength, which can also be written as $(E_z^{2\omega})/(E_x^{\omega})^2 = \sigma_{AH}^{NL}/\sigma_{zz}E_x^{\omega}$, where ($\sigma_{zz}$ being the linear c-axis conductivity and σ_{AH}^{NL} is the nonlinear anomalous Hall conductivity element zx), scales in the same way as anomalous Hall conductivity σ_{AH} in the ordinary (linear) AHE [78, 84, 62]. For the latter, σ_{AH} consists of intrinsic Berry curvature, skew-scattering, and side-jump(-like) scattering contributions [85]. The intrinsic part does not depend on longitudinal conductivity (scales with σ_{xx}^0), while upon changing temperature, skew-scattering scales with σ_{xx}^2 and side-jump contains terms that scale with σ_{xx}^0, σ_{xx}^1, and σ_{xx}^2 [84, 62, 86, 87]. It is therefore not possible to distinguish between the various mechanisms by scaling analysis. Nonetheless, it is generally understood that skew-scattering dominates for highly conducting samples with large residual conductivity [88].

4.4.4 Analysis of large NLAHE

To further our understanding, we have fit all our data for $E_z^{2\omega}/(E_x^{\omega})^2$ above T_L to the functional form: $A\sigma_{xx}^2 + B$, and the extracted A and B values are plotted in the lower panels of Fig. 4.8 as a function of the residual conductivity σ_{xx0} of the sample/axis. The upper panel shows a representative fitting for the 127-nm-thick sample with I‖a.

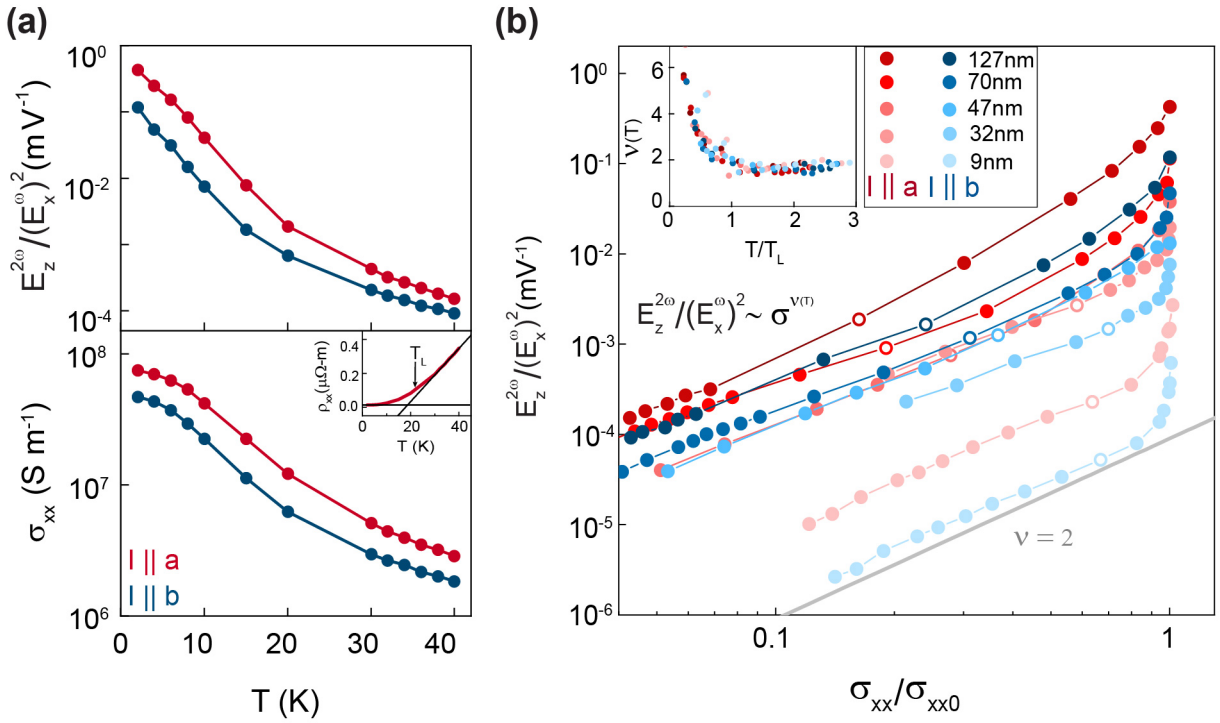

Figure 4.6: **Scaling of the NLAHE with sample conductivity.** **(a)** Main panel: $E_z^{2\omega}/(E_x^{\omega})^2$ and σ_{xx} vs. temperature for I‖a and I‖b in 127-nm-thick sample. Inset: longitudinal resistivity ρ_{xx} vs. temperature for I‖a in same sample. ρ_{xx} crosses over from linear temperature dependence to saturation below T_L ∼18K. **(b)** Main panel: $E_z^{2\omega}/(E_x^{\omega})^2$ vs. σ_{xx}/σ_{xx0} for all four samples along a and b axes. All traces show scaling close to a power law with exponent of 2 at lower conductivity (higher temperature) and exhibits an upturn as σ_{xx} approaches σ_{xx0}. Open circles mark the data points taken at the temperature closest to T_L. Inset: local scaling exponent ν vs. temperature. ν continually increases above 2 for all traces below T_L.

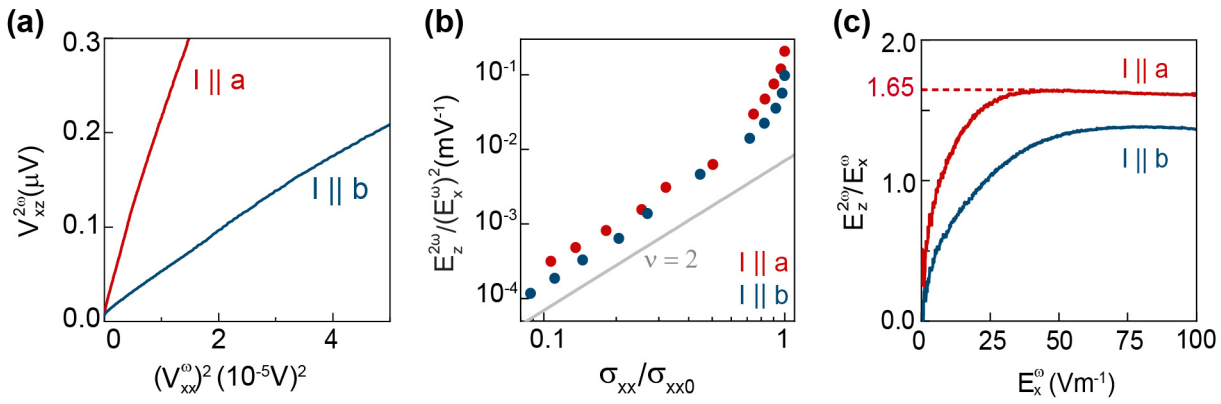

Figure 4.7: **Measurement of c-axis NLAHE in bulk-like WTe_2. (a)** Second harmonic V_{xz} vs. first harmonic V_{xx}^2 for I‖a and I‖b in 130-nm-thick sample at 2K. **b** NLAHE strength $E_z^{2\omega}/(E_x^{2\omega})^2$ vs. σ_{xx}/σ_{xx0} for I‖a and I‖b. c, Hall angle $E_z^{2\omega}/E_x^{2\omega}$ vs $E_x^{2\omega}$ for I‖a and I‖b. Peak NLAHE strength and Hall angle is less than but comparable to 127-nm-thick $MoTe_2$.

A initially decreases with increasing σ_{xx0}, but saturates at higher σ_{xx0}. For the AHE, the skew-scattering term is given by $A = \alpha\sigma_{xx0}^{-1}$ [84, 62, 89, 87], where α is termed the skew-scattering coefficient and the residual conductivity is taken as a measure of the disorder from impurities. This general scaling cannot be directly applied for our samples, since we are not tuning the impurity concentration by changing thickness, while measurements along the different crystalline axes for the same sample show different residual conductivity due to differences in band structure, not disorder. By reducing thickness, we have instead increased the contribution of surface scattering to the total resistivity, which by Matthiessen's rule can be written as: $\sigma_{xx0}^{-1} = \sigma_{xx0b(ulk)}^{-1} + \sigma_{xx0s(urface)}^{-1}$. Taking into account the different symmetries for the bulk and surface layers, we further assign different skew scattering coefficients between the two, and write: $A = \alpha_b\sigma_{xx0b}^{-1} + \alpha_s{\sigma_{xx0s}}^{-1} = \alpha_s{\sigma_{xx0}}^{-1} + (\alpha_b - \alpha_s){\sigma_{xx0b}}^{-1}$. In the thick limit, we expect $\sigma_{xx0} \sim \sigma_{xx0b}$, and so A $\sim \alpha_b\sigma_{xx0b}^{-1}$, consistent with the nonzero constant value we observe at high conductivity. If we further approximate that σ_{xx0b} is independent of thickness and equal to the measured σ_{xx0} of our thickest sample, we can fit our data across the entire thickness (residual conductivity) range for each axis to the formula above (see colored lines in the middle panel of Fig. 4.8). The extracted skew-

scattering coefficients are shown in the inset. Overall, α is larger for bulk skew-scattering and similar between the two axes.

The constant term B is expected to contain contributions both from the intrinsic Berry curvature and extrinsic side-jump(-like) events and be independent of residual conductivity [62, 89, 90]. Although this value varies over two orders of magnitude between samples, we indeed do not observe any clear trend with σ_{xx0}. We first calculate the upper limit for the predicted intrinsic contribution to B in the section below.

Calculation of intrinsic contribution

In the NLAHE, the vertical Hall current is given by $j_z^{2\omega} = \sigma_{zz} E_z^{2\omega} = 2\chi_{zxx}(E_x^{\omega})^2$, where χ_{zxx} is the nonlinear susceptibility tensor given by [75],

$$\chi_{zxx} = -\epsilon_{zyx} \frac{e^3 \tau}{2\hbar^2(1 + i\omega\tau)} D_{xy}$$

where ϵ_{zyx} is the third-rank Levi-Civita symbol and D_{xy} is the intrinsic Berry curvature dipole. In the DC limit $\omega << 1$, we have: $\frac{E_z^{2\omega}}{(E_x^{\omega})^2} = \frac{1}{\sigma_{zz}} \frac{e^3\tau}{\hbar^2} D_{xy}$.

For each sample, we have extracted the electron and hole densities (n, p) and mobilities (μ_n, μ_p) using a two-band model for the ordinary Hall effect and magnetoresistance [10]. As we saw in the previous chapter, the electron and hole densities are nearly balanced. We can then obtain the corresponding scattering time, $\tau = \frac{\mu m_{eff}}{e}$, where $m_{eff} \sim m_0$, the bare electron mass [10]. τ ranges between ~0.2ps (9nm) to ~1ps (127nm).

We used both experimental c-axis measurement and DFT calculation to determine $\sigma_{zz} \sim 0.6\sigma_{xx}$ for I‖a near the charge neutrality point, while the theoretical value for D_{xy} is 0.856 [10]. From these values, we calculate an upper limit of $E_z^{2\omega}/(E_x^{\omega})^2 = 1.3 \times 10^{-7} m/V$ across all our different samples the result is marked by the gray line. This theoretical value is one order of magnitude less than our smallest experimental value, suggesting that intrinsic Berry curvature only plays a minor role in the extremely large NLAHE observed here. Although, the intrinsic contribution may in principle be enhanced by external perturbations, such as strain, or symmetry breaking by the surface layers [91, 92, 93].

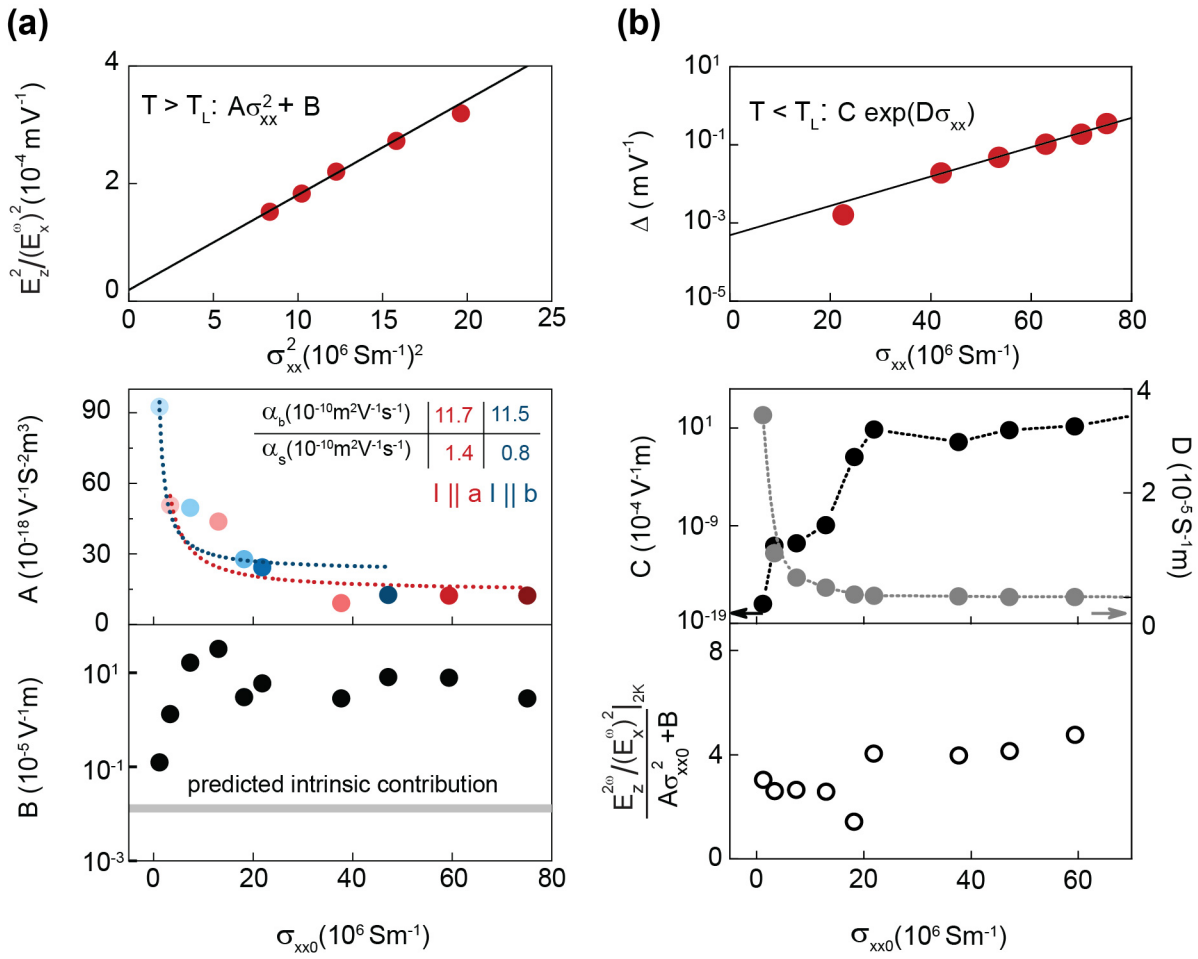

Figure 4.8: **Determination and analysis of scaling parameters in NLAHE. (a)** Upper panel: representative fit to $E_z^{2\omega}/(E_x^{\omega})^2 = A\sigma_{xx}^2 + B$ for $T > T_L$ for 127-nm-thick sample, a-axis. Lower panels: A and B vs.σ_{xx0} for all samples and axes. Red and blue dashed lines are fits to formulas described in the text for a and b axes, respectively. Gray line is predicted intrinsic Berry curvature contribution to B. **(b)** Upper panel: representative fit to $\Delta = Cexp(D\sigma_{xx})$ for $T < T_L$ for 127-nm-thick sample, a-axis. Middle panel: C and D vs. σ_{xx0} for all samples and axes. Lower panel: low-temperature enhancement factor $(E_z^{2\omega})/(E_x^{\omega})^2\Big|_{2K}/(A\sigma_{xx0}^2 + B)$ vs. σ_{xx0}.

For temperatures below T_L, $E_z^{2\omega}/(E_x^{\omega})^2$ increases further with conductivity beyond the σ_{xx}^2 dependence seen at higher temperatures (see Fig. 4.6b). Such behavior has not been previously observed experimentally for the AHE, and so it remains an open theoretical question as to the microscopic scattering mechanism responsible for this effect. A possible candidate is side-jump, as it has been recently predicted that, for high-purity samples below the Debye or Bloch-Gruneisen temperature, scaling parameters for side-jump(-like) contributions may actually be temperature-dependent [62]. We proceed to fit our data in this regime in order to determine an empirical scaling relationship. The continuous increase of ν below T_L suggests an exponential dependence on σ_{xx}, and so we have fit the additional contribution to: $\Delta(E_z^{2\omega})/(E_x^{\omega})^2 - (A\sigma_{xx}^2 + B) = Cexp(D\sigma_{xx})$, and the extracted C and D values are plotted in the middle panel of Fig. 4.8b as a function of the residual conductivity σ_{xx0} of the sample/axis. The upper panel shows a representative fitting for the 127-nm-thick sample with I‖a. While C sharply with increasing σ_{xx0}, D decreases. The net effect, however, is such that the NLAHE strength at low temperature is increased by a roughly constant factor above that expected from skew-scattering alone. In the lower panel of Fig. 4.8b, we have plotted as a function of σ_{xx0}, the ratio between the measured $E_z^{2\omega}/(E_x^{\omega})^2$ value at 2K and $A\sigma_{xx0}^2 + B$, the extrapolated skew-contribution, and this factor falls between 3–5 for all but one sample/axis.

4.5 Discussions

The combination of the different scattering processes, together with the nonlinear dependence of the Hall field on applied bias, allows us to obtain the largest Hall ratio in electric field observed to date outside the quantum (anomalous) Hall regime. In Fig. 4.9a, we have plotted $E_z^{2\omega}/E_x^{\omega}$, the ratio between the Hall field generated and the applied longitudinal field, as a function of E_x^{ω} measured for the 127-nm-thick sample at 2K, which shows the largest NLAHE strength amongst all our samples. The ratio is always larger for I‖a, for which it rises initially with increasing E_x^{ω}, reaching a maximum of 2.47, an order of magnitude larger than the analogous quantity measured in giant linear AHE compounds [94, 95]. At larger bias, $E_z^{2\omega}/E_x^{\omega}$ decreases as E_x^{ω} itself becomes sublinear with applied current, likely due to heating.

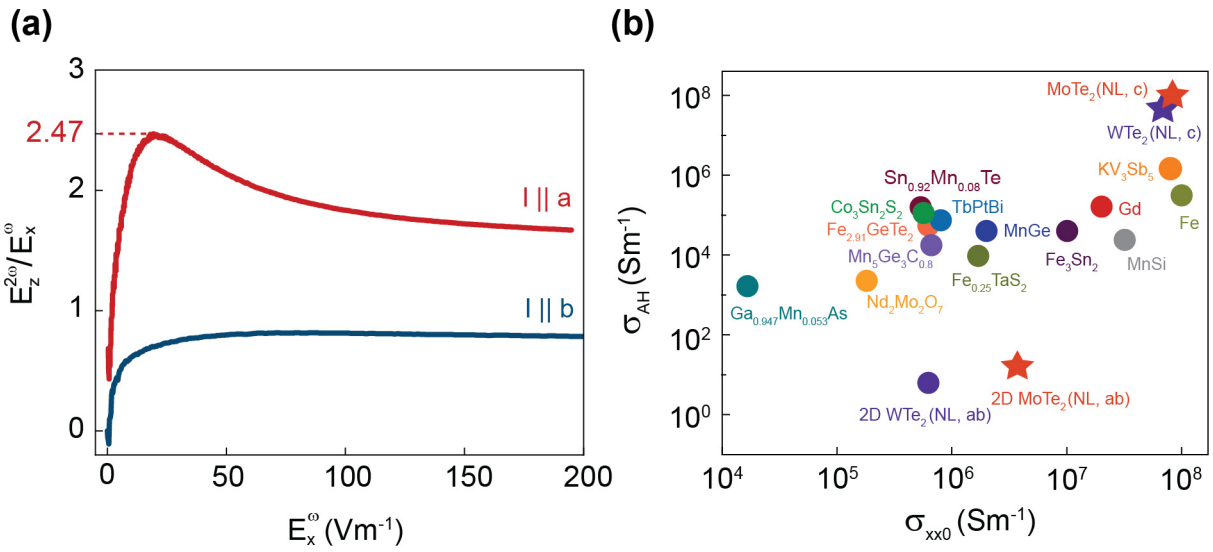

Figure 4.9: **Observation of extremely large Hall ratio and conductivity at higher bias.** **(a)** Hall ratio $E_z^{2\omega}/E_x^{\omega}$ vs E_x^{ω} for I‖a and I‖b in 127-nm-thick sample. Hall ratio reaches 2.83 for a-axis. **(b)** Anomalous Hall conductivity σ_{AH} vs. σ_{xx0} for various linear and nonlinear AHE materials. Stars mark values measured in this study.

We would further like to quantify the nonlinear anomalous Hall conductivity at this peak Hall ratio, which can be expressed as: $\sigma_{AH}^{NL} = (E_z^{2\omega}/E_x^{\omega})\sigma_{zz}$. We have measured both the a- and c-axis resistivity of a separate bulk $MoTe_2$ crystal (grown under the same conditions as that used for our devices) and further calculated the conductivity anisotropy as a function of the position of the Fermi level using density functional theory. σ_{zz}/σ_{xx} ~0.25(exp.)-0.6(th.) for I‖a near the charge neutrality point where electrons and holes compensate, yielding σ_{AH}^{NL} ~8×10^7 S/m. Assuming a similar anisotropy ratio for WTe_2, we estimate σ_{AH}^{NL} ~5×10^7 S/m at the peak Hall ratio for our bulk-like WTe_2 device. For comparison, we have plotted these values in Fig. 4.9b, together with those measured in-plane for ultrathin $MoTe_2$ and WTe_2, as well as the linear anomalous Hall conductivities measured in various magnetic systems as a function of the residual longitudinal conductivity [96, 97, 63, 98, 32, 99, 100, 101, 102, 103, 104]. Overall, σ_{AH} is larger in more highly conducting systems. The values for the c-axis response in $MoTe_2$ and WTe_2, in particular, are the largest yet reported.

In summary, we have observed an extremely large c-axis NLAHE in T_d-$MoTe_2$ that is dominated by asymmetric electron scattering. Our work reaffirms the importance of extrinsic contributions to the (NL)AHE, especially in highly conducting metals, and opens a new direction for obtaining giant Hall ratios and conductivities in non-centrosymmetric systems without breaking time reversal symmetry.

Chapter 5

Conclusion and Outlook

This thesis was aimed at exploring the interplay between crystal structure and magneto-transport in semimetallic transition metal dichalogenides (TMDCs). We started with a discussion on relevant layered materials, namely, graphene, boron nitride, and semimetallic TMDCs: $MoTe_2$ and WTe_2. We learned that these semimetallic TMDCs can exhibit a large magnetoresistance and non-linear phenomena owing to their unique structural and electronic properties. Then, we discussed the techniques that can be used to assemble heterostructures of layered materials for transport measurements.

We studied the thickness evolution of magnetoresistance in T_d-$MoTe_2$. We measured a large magnetoresistance of $\sim$3000% in a 180nm sample, which decreases by two orders of magnitude upon reducing the thickness to 7nm. This occurs concomitantly with a decrease in the carrier mobility, and electron-hole imbalance upon reducing the thickness. The question we tried to address is which of these two factors is dominant in suppressing the magnetoresistance in thinner samples. We performed both classical magnetotransport and quantum oscillation measurements to study carrier transport, and identify signatures of electron(hole) pockets on the Fermi surface. We used a two-band model analysis for magnetoresistance, and calculated the associated carrier mobility and electron-hole ratio. After comparing our data across various thicknesses, we arrived to a conclusion that magnetoresistance is more sensitive to the mobility, therefore, a large magnetoresistance can still be achieved with some degree of carrier imbalance. In principle, a MR of about 1000%

can be achieved, despite the carrier imbalance ratio of 0.8, if a high mobility can be maintained. Thin layers isolated from high quality single crystals will have a higher mobility, which can further be increased by fabricating the device on atomically flat boron nitride substrate. We also observed oscillations in longitudinal resistivity for higher magnetic field (>6T). The two prominent oscillations at frequencies 202T and 266T, correspond to the electron pockets on the Fermi surface as seen in density functional theory calculations.

Then, we looked into the non-linear anomalous Hall effect (NLAHE) exhibited by $MoTe_2$ and WTe_2, arising from their non-centrosymmetric crystal structure. Here, we perform both in-plane and out-of-plane, first and second harmonic transport measurements to study the NLAHE. We present a scaling relation between $E_z^{2\omega}/(E_x^{\omega})^2$ and longitudinal conductivity, to determine various contributions to the NLAHE. From the scaling, we find that it has mainly three types of dependency on the conductivity, namely, B, $A\sigma_{xx}^2$, and $Cexp(D\sigma_{xx}/\sigma_{xx0})$, indicating the contributions from intrinsic plus side jump mechanism, skew-scattering, and an unexplored exponential scattering, respectively. The Hall ratio was $(E_z^{2\omega}/E_x^{\omega})$ measured to be 2.47 and 1.85, for $MoTe_2$ and WTe_2, respectively. The corresponding Hall conductivity values are 8×10^7 and 5×10^7 for $MoTe_2$ and WTe_2, respectively. The Hall ratio measured in $MoTe_2$ is the largest outside of the quantum Hall regime, and Hall conductivity is largest yet achieved in any material.

From the measurements on the non-linear anomalous Hall effect, we further continue to address the mechanism behind the exponential variation of NLAHE strength with longitudinal conductivity in the temperature range below 15K. We have designed a geometry to examine if there is a spin dependent mechanism responsible for this large effect. To investigate the spin accumulation on one of top and bottom surfaces of bulk $MoTe_2$, we will measure the spin filtering using a ferromagnetic potential barrier.

References

[1] Andrea Splendiani, Liang Sun, Yuanbo Zhang, Tianshu Li, Jonghwan Kim, Chi Yung Chim, Giulia Galli, and Feng Wang. Emerging photoluminescence in monolayer MoS2. *Nano Letters*, 2010.

[2] O. P. Sushkov, A. I. Milstein, M. Mori, and S. Maekawa. Does the side jump effect exist?, 2012.

[3] Manish Chhowalla, Hyeon Suk Shin, Goki Eda, Lain Jong Li, Kian Ping Loh, and Hua Zhang. The chemistry of two-dimensional layered transition metal dichalcogenide nanosheets, 2013.

[4] K. S. Novoselov, A. K. Geim, S. V. Morozov, D. Jiang, Y. Zhang, S. V. Dubonos, I. V. Grigorieva, and A. A. Firsov. Electric field in atomically thin carbon films. *Science*, 2004.

[5] K. S. Novoselov, D. Jiang, F. Schedin, T. J. Booth, V. V. Khotkevich, S. V. Morozov, and A. K. Geim. Two-dimensional atomic crystals. *Proceedings of the National Academy of Sciences of the United States of America*, 2005.

[6] Yuan Cao, Valla Fatemi, Shiang Fang, Kenji Watanabe, Takashi Taniguchi, Efthimios Kaxiras, and Pablo Jarillo-Herrero. Unconventional superconductivity in magic-angle graphene superlattices. *Nature*, 2018.

[7] Aaron L. Sharpe, Eli J. Fox, Arthur W. Barnard, Joe Finney, Kenji Watanabe, Takashi Taniguchi, M. A. Kastner, and David Goldhaber-Gordon. Emergent ferromagnetism near three-quarters filling in twisted bilayer graphene. *Science*, 2019.

[8] Guorui Chen, Aaron L. Sharpe, Eli J. Fox, Ya Hui Zhang, Shaoxin Wang, Lili Jiang, Bosai Lyu, Hongyuan Li, Kenji Watanabe, Takashi Taniguchi, Zhiwen Shi, T. Senthil, David Goldhaber-Gordon, Yuanbo Zhang, and Feng Wang. Tunable correlated Chern insulator and ferromagnetism in a moiré superlattice. *Nature*, 2020.

[9] Mazhar N. Ali, Jun Xiong, Steven Flynn, Jing Tao, Quinn D. Gibson, Leslie M. Schoop, Tian Liang, Neel Haldolaarachchige, Max Hirschberger, N. P. Ong, and R. J. Cava. Large, non-saturating magnetoresistance in WTe2. *Nature*, 2014.

[10] Shazhou Zhong, Archana Tiwari, George Nichols, Fangchu Chen, Xuan Luo, Yuping Sun, and Adam W. Tsen. Origin of magnetoresistance suppression in thin γ-MoT e2. *Physical Review B*, 97(24):1–5, 2018.

[11] F. C. Chen, H. Y. Lv, X. Luo, W. J. Lu, Q. L. Pei, G. T. Lin, Y. Y. Han, X. B. Zhu, W. H. Song, and Y. P. Sun. Extremely large magnetoresistance in the type-II Weyl semimetal MoTe2. *Physical Review B*, 2016.

[12] Alexey A. Soluyanov, Dominik Gresch, Zhijun Wang, Quansheng Wu, Matthias Troyer, Xi Dai, and B. Andrei Bernevig. Type-II Weyl semimetals. *Nature*, 2015.

[13] J. Jiang, Z. K. Liu, Y. Sun, H. F. Yang, C. R. Rajamathi, Y. P. Qi, L. X. Yang, C. Chen, H. Peng, C. C. Hwang, S. Z. Sun, S. K. Mo, I. Vobornik, J. Fujii, S. S.P. Parkin, C. Felser, B. H. Yan, and Y. L. Chen. Signature of type-II Weyl semimetal phase in MoTe 2. *Nature Communications*, 8, 2017.

[14] Ke Deng, Guoliang Wan, Peng Deng, Kenan Zhang, Shijie Ding, Eryin Wang, Mingzhe Yan, Huaqing Huang, Hongyun Zhang, Zhilin Xu, Jonathan Denlinger, Alexei Fedorov, Haitao Yang, Wenhui Duan, Hong Yao, Yang Wu, Shoushan Fan, Haijun Zhang, Xi Chen, and Shuyun Zhou. Experimental observation of topological Fermi arcs in type-II Weyl semimetal MoTe 2. *Nature Physics*, 12(12):1105–1110, 2016.

[15] Jian Cui, Peiling Li, Jiadong Zhou, Wen Yu He, Xiangwei Huang, Jian Yi, Jie Fan, Zhongqing Ji, Xiunian Jing, Fanming Qu, Zhi Gang Cheng, Changli Yang, Li Lu, Kazu Suenaga, Junwei Liu, Kam Tuen Law, Junhao Lin, Zheng Liu, and

Guangtong Liu. Transport evidence of asymmetric spin–orbit coupling in few-layer superconducting 1T d -MoTe 2. *Nature Communications*, 2019.

[16] J. Jiang, F. Tang, X. C. Pan, H. M. Liu, X. H. Niu, Y. X. Wang, D. F. Xu, H. F. Yang, B. P. Xie, F. Q. Song, P. Dudin, T. K. Kim, M. Hoesch, P. Kumar Das, I. Vobornik, X. G. Wan, and D. L. Feng. Signature of strong spin-orbital coupling in the large nonsaturating magnetoresistance material wte_2. *Phys. Rev. Lett.*, 115:166601, Oct 2015.

[17] Yanpeng Qi, Pavel G. Naumov, Mazhar N. Ali, Catherine R. Rajamathi, Walter Schnelle, Oleg Barkalov, Michael Hanfland, Shu Chun Wu, Chandra Shekhar, Yan Sun, Vicky Süß, Marcus Schmidt, Ulrich Schwarz, Eckhard Pippel, Peter Werner, Reinald Hillebrand, Tobias Förster, Erik Kampert, Stuart Parkin, R. J. Cava, Claudia Felser, Binghai Yan, and Sergey A. Medvedev. Superconductivity in Weyl semimetal candidate MoTe2. *Nature Communications*, 7:1–7, 2016.

[18] Ebrahim Sajadi, Tauno Palomaki, Zaiyao Fei, Wenjin Zhao, Philip Bement, Christian Olsen, Silvia Luescher, Xiaodong Xu, Joshua A. Folk, and David H. Cobden. Gate-induced superconductivity in a monolayer topological insulator. *Science*, 2018.

[19] Wudi Wang, Stephan Kim, Minhao Liu, F. A. Cevallos, R. J. Cava, and N. P. Ong. Evidence for an edge supercurrent in the Weyl superconductor MoTe2. *Science*, 2020.

[20] Li Kun Shi and Justin C.W. Song. Symmetry, spin-texture, and tunable quantum geometry in a WTe2 monolayer. *Physical Review B*, 2019.

[21] Zaiyao Fei, Tauno Palomaki, Sanfeng Wu, Wenjin Zhao, Xinghan Cai, Bosong Sun, Paul Nguyen, Joseph Finney, Xiaodong Xu, and David H. Cobden. Edge conduction in monolayer WTe 2. *Nature Physics*, 2017.

[22] R. Peierls. Quelques propriétés typiques des corps solides. *Annales de l'I.H.P.*, 1935.

[23] L. D. Landau. Zur Th eorie der phasenumwandlungen II. *Phys. Z. Sowjetunion*, 1937.

[24] N. D. Mermin. Crystalline order in two dimensions. *Physical Review*, 1968.

[25] J. A. Venables, G. D.T. Spiller, and M. Hanbucken. Nucleation and growth of thin films, 1984.

[26] J. W. Evans, P. A. Thiel, and M. C. Bartelt. Morphological evolution during epitaxial thin film growth: Formation of 2D islands and 3D mounds, 2006.

[27] Kenji Watanabe, Takashi Taniguchi, and Hisao Kanda. Direct-bandgap properties and evidence for ultraviolet lasing of hexagonal boron nitride single crystal. *Nature Materials*, 2004.

[28] J. A. Wilson and A. D. Yoffe. The transition metal dichalcogenides discussion and interpretation of the observed optical, electrical and structural properties. *Advances in Physics*, 1969.

[29] Kin Fai Mak, Changgu Lee, James Hone, Jie Shan, and Tony F. Heinz. Atomically thin MoS2: A new direct-gap semiconductor. *Physical Review Letters*, 2010.

[30] Qing Hua Wang, Kourosh Kalantar-Zadeh, Andras Kis, Jonathan N. Coleman, and Michael S. Strano. Electronics and optoelectronics of two-dimensional transition metal dichalcogenides, 2012.

[31] Yan Sun, Shu Chun Wu, and Binghai Yan. Topological surface states and Fermi arcs of the noncentrosymmetric Weyl semimetals TaAs, TaP, NbAs, and NbP. *Physical Review B - Condensed Matter and Materials Physics*, 2015.

[32] Zhijun Wang, Dominik Gresch, Alexey A. Soluyanov, Weiwei Xie, S. Kushwaha, Xi Dai, Matthias Troyer, Robert J. Cava, and B. Andrei Bernevig. MoTe2: A Type-II Weyl Topological Metal. *Physical Review Letters*, 2016.

[33] Lunan Huang, Timothy M. McCormick, Masayuki Ochi, Zhiying Zhao, Michi To Suzuki, Ryotaro Arita, Yun Wu, Daixiang Mou, Huibo Cao, Jiaqiang Yan, Nandini Trivedi, and Adam Kaminski. Spectroscopic evidence for a type II Weyl semimetallic state in MoTe 2. *Nature Materials*, 2016.

[34] A. Tamai, Q. S. Wu, I. Cucchi, F. Y. Bruno, S. Riccò, T. K. Kim, M. Hoesch, C. Barreteau, E. Giannini, C. Besnard, A. A. Soluyanov, and F. Baumberger. Fermi

arcs and their topological character in the candidate type-II Weyl semimetal MoTe2. *Physical Review X*, 2016.

[35] Ke Deng, Guoliang Wan, Peng Deng, Kenan Zhang, Shijie Ding, Eryin Wang, Mingzhe Yan, Huaqing Huang, Hongyun Zhang, Zhilin Xu, Jonathan Denlinger, Alexei Fedorov, Haitao Yang, Wenhui Duan, Hong Yao, Yang Wu, Shoushan Fan, Haijun Zhang, Xi Chen, and Shuyun Zhou. Experimental observation of topological Fermi arcs in type-II Weyl semimetal MoTe 2. *Nature Physics*, 2016.

[36] N. Xu, Z. J. Wang, A. P. Weber, A. Magrez, P. Bugnon, H. Berger, C. E. Matt, J. Z. Ma, B. B. Fu, B. Q. Lv, N. C. Plumb, M. Radovic, E. Pomjakushina, K. Conder, T. Qian, J. H. Dil, J. Mesot, H. Ding, and M. Shi. Discovery of weyl semimetal state violating lorentz invariance in mote2, 2016.

[37] Dong Hoon Keum, Suyeon Cho, Jung Ho Kim, Duk Hyun Choe, Ha Jun Sung, Min Kan, Haeyong Kang, Jae Yeol Hwang, Sung Wng Kim, Heejun Yang, K. J. Chang, and Young Hee Lee. Bandgap opening in few-layered monoclinic MoTe 2. *Nature Physics*, 2015.

[38] Rafi Bistritzer and Allan H. MacDonald. Moiré bands in twisted double-layer graphene. *Proceedings of the National Academy of Sciences of the United States of America*, 108(30):12233–12237, 2011.

[39] Stephen Carr, Shiang Fang, and Efthimios Kaxiras. Electronic-structure methods for twisted moiré layers. *Nature Reviews Materials*, 5(10):748–763, 2020.

[40] Matthew Yankowitz, Shaowen Chen, Hryhoriy Polshyn, Yuxuan Zhang, K. Watanabe, T. Taniguchi, David Graf, Andrea F. Young, and Cory R. Dean. Tuning superconductivity in twisted bilayer graphene. *Science*, 2019.

[41] D. G. Purdie, N. M. Pugno, T. Taniguchi, K. Watanabe, A. C. Ferrari, and A. Lombardo. Cleaning interfaces in layered materials heterostructures. *Nature Communications*, 2018.

[42] Qiong Zhou, D. Rhodes, Q. R. Zhang, S. Tang, R. Schönemann, and L. Balicas. Hall effect within the colossal magnetoresistive semimetallic state of MoTe2. *Physical Review B*, 2016.

[43] Yongkang Luo, H. Li, Y. M. Dai, H. Miao, Y. G. Shi, H. Ding, A. J. Taylor, D. A. Yarotski, R. P. Prasankumar, and J. D. Thompson. Hall effect in the extremely large magnetoresistance semimetal WTe2. *Applied Physics Letters*, 2015.

[44] Valla Fatemi, Quinn D. Gibson, Kenji Watanabe, Takashi Taniguchi, Robert J. Cava, and Pablo Jarillo-Herrero. Magnetoresistance and quantum oscillations of an electrostatically tuned semimetal-to-metal transition in ultrathin WTe2. *Physical Review B*, 2017.

[45] S. Thirupathaiah, Rajveer Jha, Banabir Pal, J. S. Matias, P. Kumar Das, P. K. Sivakumar, I. Vobornik, N. C. Plumb, M. Shi, R. A. Ribeiro, and D. D. Sarma. MoTe2: An uncompensated semimetal with extremely large magnetoresistance. *Physical Review B*, 2017.

[46] I. Pletikosić, Mazhar N. Ali, A. V. Fedorov, R. J. Cava, and T. Valla. Electronic structure basis for the extraordinary magnetoresistance in WTe2. *Physical Review Letters*, 2014.

[47] Rui He, Shazhou Zhong, Hyun Ho Kim, Gaihua Ye, Zhipeng Ye, Logan Winford, Daniel McHaffie, Ivana Rilak, Fangchu Chen, Xuan Luo, Yuping Sun, and Adam W. Tsen. Dimensionality-driven orthorhombic MoT e2 at room temperature. *Physical Review B*, 2018.

[48] Kyounghwan Kim, Ashley DaSilva, Shengqiang Huang, Babak Fallahazad, Stefano Larentis, Takashi Taniguchi, Kenji Watanabe, Brian J. LeRoy, Allan H. MacDonald, and Emanuel Tutuc. Tunable moiré bands and strong correlations in small-twist-angle bilayer graphene. *Proceedings of the National Academy of Sciences of the United States of America*, 2017.

[49] D. Rhodes, D. A. Chenet, B. E. Janicek, C. Nyby, Y. Lin, W. Jin, D. Edelberg, E. Mannebach, N. Finney, A. Antony, T. Schiros, T. Klarr, A. Mazzoni, M. Chin,

Y. C. Chiu, W. Zheng, Q. R. Zhang, F. Ernst, J. I. Dadap, X. Tong, J. Ma, R. Lou, S. Wang, T. Qian, H. Ding, R. M. Osgood, D. W. Paley, A. M. Lindenberg, P. Y. Huang, A. N. Pasupathy, M. Dubey, J. Hone, and L. Balicas. Engineering the Structural and Electronic Phases of MoTe2 through W Substitution. *Nano Letters*, 2017.

[50] Kyoo Kim, Junho Seo, Eunwoo Lee, K. T. Ko, B. S. Kim, Bo Gyu Jang, Jong Mok Ok, Jinwon Lee, Youn Jung Jo, Woun Kang, Ji Hoon Shim, C. Kim, Han Woong Yeom, Byung Il Min, Bohm Jung Yang, and Jun Sung Kim. Large anomalous Hall current induced by topological nodal lines in a ferromagnetic van der Waals semimetal. *Nature Materials*, 2018.

[51] van Alphen P M de Haas W J. *Proc. Neth. R. Acad. Sci.*, (33):1106, 1930.

[52] D. Shoenberg. Magnetic oscillations in metals. 1984.

[53] J. E. Moore and J. Orenstein. Confinement-induced berry phase and helicity-dependent photocurrents. *Physical Review Letters*, 105(2):1–4, 2010.

[54] Zhurun Ji, Gerui Liu, Zachariah Addison, Wenjing Liu, Peng Yu, Heng Gao, Zheng Liu, Andrew M. Rappe, Charles L. Kane, Eugene J. Mele, and Ritesh Agarwal. Spatially dispersive circular photogalvanic effect in a Weyl semimetal. *Nature Materials*, 2019.

[55] Kaifei Kang, Tingxin Li, Egon Sohn, Jie Shan, and Kin Fai Mak. Nonlinear anomalous Hall effect in few-layer WTe 2. *Nature Materials*, 18(4):324–328, 2019.

[56] Qiong Ma, Su Yang Xu, Huitao Shen, David MacNeill, Valla Fatemi, Tay Rong Chang, Andrés M. Mier Valdivia, Sanfeng Wu, Zongzheng Du, Chuang Han Hsu, Shiang Fang, Quinn D. Gibson, Kenji Watanabe, Takashi Taniguchi, Robert J. Cava, Efthimios Kaxiras, Hai Zhou Lu, Hsin Lin, Liang Fu, Nuh Gedik, and Pablo Jarillo-Herrero. Observation of the nonlinear Hall effect under time-reversal-symmetric conditions. *Nature*, 565(7739):337–342, 2019.

[57] O. O. Shvetsov, V. D. Esin, A. V. Timonina, N. N. Kolesnikov, and E. V. Deviatov. Nonlinear Hall Effect in Three-Dimensional Weyl and Dirac Semimetals. *JETP Letters*, 2019.

[58] Sheng Chin Ho, Ching Hao Chang, Yu Chiang Hsieh, Shun Tsung Lo, Botsz Huang, Thi Hai Yen Vu, Carmine Ortix, and Tse Ming Chen. Zero-magnetic-field hall effects in artificially corrugated bilayer graphene, 2019.

[59] Meizhen Huang, Zefei Wu, Jinxin Hu, Xiangbin Cai, En Li, Liheng An, Xuemeng Feng, Ziqing Ye, Nian Lin, Kam Tuen Law, and Ning Wang. Giant nonlinear Hall effect in twisted WSe2, 2020.

[60] Su Yang Xu, Qiong Ma, Yang Gao, Anshul Kogar, Alfred Zong, Andrés M. Mier Valdivia, Thao H. Dinh, Shin Ming Huang, Bahadur Singh, Chuang Han Hsu, Tay Rong Chang, Jacob P.C. Ruff, Kenji Watanabe, Takashi Taniguchi, Hsin Lin, Goran Karapetrov, Di Xiao, Pablo Jarillo-Herrero, and Nuh Gedik. Spontaneous gyrotropic electronic order in a transition-metal dichalcogenide. *Nature*, 2020.

[61] Inti Sodemann and Liang Fu. Quantum Nonlinear Hall Effect Induced by Berry Curvature Dipole in Time-Reversal Invariant Materials. *Physical Review Letters*, 115(21):1–5, 2015.

[62] Cong Xiao, Hailong Zhou, and Qian Niu. Scaling parameters in anomalous and nonlinear Hall effects depend on temperature. *Physical Review B*, 2019.

[63] Shuo Ying Yang, Yaojia Wang, Brenden R. Ortiz, Defa Liu, Jacob Gayles, Elena Derunova, Rafael Gonzalez-Hernandez, Libor Šmejkal, Yulin Chen, Stuart S.P. Parkin, Stephen D. Wilson, Eric S. Toberer, Tyrel McQueen, and Mazhar N. Ali. Giant, unconventional anomalous Hall effect in the metallic frustrated magnet candidate, KV3Sb5. *Science Advances*, 2020.

[64] Yukako Fujishiro, Naoya Kanazawa, Ryosuke Kurihara, Hiroaki Ishizuka, Tomohiro Hori, Fehmi Sami Yasin, Xiuzhen Yu, Atsushi Tsukazaki, Masakazu Ichikawa, Masashi Kawasaki, Naoto Nagaosa, Masashi Tokunaga, and Yoshinori Tokura. Giant anomalous Hall effect from spin-chirality scattering in a chiral magnet. *Nature Communications*, 2021.

[65] D. Maryenko, A. S. Mishchenko, M. S. Bahramy, A. Ernst, J. Falson, Y. Kozuka, A. Tsukazaki, N. Nagaosa, and M. Kawasaki. Observation of anomalous Hall effect in a non-magnetic two-dimensional electron system. *Nature Communications*, 2017.

[66] Robert Karplus and J. M. Luttinger. Hall effect in ferromagnetics. *Physical Review*, 95(5):1154–1160, 1954.

[67] M . V . Berry. Quantal Phase Factors Accompanying Adiabatic Changes Author (s): Source : . Series A , Mathematical and Physical Published by : The Royal Society Stable URL : http://www.jstor.org/stable/2397741. *Proceedings of the Royal Society of London*, 392(1802):45–57, 1984.

[68] Ming Che Chang and Qian Niu. Berry phase, hyperorbits, and the Hofstadter spectrum: Semiclassical dynamics in magnetic Bloch bands. *Physical Review B - Condensed Matter and Materials Physics*, 53(11):7010–7023, 1996.

[69] Ganesh Sundaram and Qian Niu. Wave-packet dynamics in slowly perturbed crystals: gradient corrections and berry-phase effects. *Physical Review B - Condensed Matter and Materials Physics*, 1999.

[70] J. Smit. The spontaneous hall effect in ferromagnetics I. *Physica*, 1955.

[71] J. Smit. The spontaneous hall effect in ferromagnetics II. *Physica*, 1958.

[72] A. K. Majumdar and L. Berger. Hall effect and magnetoresistance in pure iron, lead, Fe-Co, and Fe-Cr dilute alloys. *Physical Review B*, 1973.

[73] P. Olbrich, S. A. Tarasenko, C. Reitmaier, J. Karch, D. Plohmann, Z. D. Kvon, and S. D. Ganichev. Observation of the orbital circular photogalvanic effect. *Physical Review B - Condensed Matter and Materials Physics*, 2009.

[74] S. D. Ganichev. Spin photocurrents in quantum wells. In *Institute of Physics Conference Series*, 2003.

[75] Yang Zhang, Jeroen Van Den Brink, Claudia Felser, and Binghai Yan. Electrically tuneable nonlinear anomalous Hall effect in two-dimensional transition-metal dichalcogenides WTe2 and MoTe2. *2D Materials*, 2018.

[76] Sobhit Singh, Jinwoong Kim, Karin M. Rabe, and David Vanderbilt. Engineering weyl phases and nonlinear hall effects in t_d-mote$_2$. *Phys. Rev. Lett.*, 125:046402, Jul 2020.

[77] Rui-Hao Li, Olle G. Heinonen, Anton A. Burkov, and Steven S.-L. Zhang. Nonlinear hall effect in weyl semimetals induced by chiral anomaly. *Phys. Rev. B*, 103:045105, Jan 2021.

[78] Kaifei Kang, Tingxin Li, Egon Sohn, Jie Shan, and Kin Fai Mak. Nonlinear anomalous Hall effect in few-layer WTe 2. *Nature Materials*, 18(4):324–328, 2019.

[79] Yang Zhang, Yan Sun, and Binghai Yan. Berry curvature dipole in Weyl semimetal materials: An ab initio study. *Physical Review B*, 97(4):41101, 2018.

[80] Jhih Shih You, Shiang Fang, Su Yang Xu, Efthimios Kaxiras, and Tony Low. Berry curvature dipole current in the transition metal dichalcogenides family. *Physical Review B*, 2018.

[81] Robert W. Boyd and Barry R. Masters. Nonlinear Optics, Third Edition. *Journal of Biomedical Optics*, 2009.

[82] Qingjun Song, Xingchen Pan, Haifeng Wang, Kun Zhang, Qinghai Tan, Pan Li, Yi Wan, Yilun Wang, Xiaolong Xu, Miaoling Lin, Xiangang Wan, Fengqi Song, and Lun Dai. The In-Plane Anisotropy of WTe2 Investigated by Angle-Dependent and Polarized Raman Spectroscopy. *Scientific Reports*, 2016.

[83] Yu Song, Ruijuan Tian, Jiulong Yang, Rui Yin, Jianlin Zhao, and Xuetao Gan. Second Harmonic Generation in Atomically Thin MoTe2. *Advanced Optical Materials*, 2018.

[84] Z. Z. Du, C. M. Wang, Shuai Li, Hai Zhou Lu, and X. C. Xie. Disorder-induced nonlinear Hall effect with time-reversal symmetry. *Nature Communications*, 2019.

[85] Naoto Nagaosa, Jairo Sinova, Shigeki Onoda, A. H. MacDonald, and N. P. Ong. Anomalous Hall effect. *Reviews of Modern Physics*, 2010.

[86] Yuan Tian, Li Ye, and Xiaofeng Jin. Proper scaling of the anomalous hall effect. *Physical Review Letters*, 103(8):1–4, 2009.

[87] Dazhi Hou, Gang Su, Yuan Tian, Xiaofeng Jin, Shengyuan A. Yang, and Qian Niu. Multivariable scaling for the anomalous hall effect. *Physical Review Letters*, 114(21):1–5, 2015.

[88] Naoto Nagaosa, Jairo Sinova, Shigeki Onoda, A. H. MacDonald, and N. P. Ong. Anomalous Hall effect. *Reviews of Modern Physics*, 82(2):1539–1592, 2010.

[89] Yuan Tian, Li Ye, and Xiaofeng Jin. Proper scaling of the anomalous hall effect. *Physical Review Letters*, 2009.

[90] Dazhi Hou, Gang Su, Yuan Tian, Xiaofeng Jin, Shengyuan A. Yang, and Qian Niu. Multivariable scaling for the anomalous hall effect. *Physical Review Letters*, 2015.

[91] Jorge I. Facio, Dmitri Efremov, Klaus Koepernik, Jhih Shih You, Inti Sodemann, and Jeroen Van Den Brink. Strongly Enhanced Berry Dipole at Topological Phase Transitions in BiTeI. *Physical Review Letters*, 2018.

[92] O. Matsyshyn and I. Sodemann. Nonlinear Hall Acceleration and the Quantum Rectification Sum Rule. *Physical Review Letters*, 2019.

[93] Joolee Son, Kyung Han Kim, Y. H. Ahn, Hyun Woo Lee, and Jieun Lee. Strain Engineering of the Berry Curvature Dipole and Valley Magnetization in Monolayer MoS2. *Physical Review Letters*, 2019.

[94] Enke Liu, Yan Sun, Nitesh Kumar, Lukas Muechler, Aili Sun, Lin Jiao, Shuo Ying Yang, Defa Liu, Aiji Liang, Qiunan Xu, Johannes Kroder, Vicky Süß, Horst Borrmann, Chandra Shekhar, Zhaosheng Wang, Chuanying Xi, Wenhong Wang, Walter Schnelle, Steffen Wirth, Yulin Chen, Sebastian T.B. Goennenwein, and Claudia Felser. Giant anomalous Hall effect in a ferromagnetic kagome-lattice semimetal. *Nature Physics*, 2018.

[95] Ratnadwip Singha, Shubhankar Roy, Arnab Pariari, Biswarup Satpati, and Prabhat Mandal. Magnetotransport properties and giant anomalous Hall angle in half-Heusler compound TbPtBi, 2019.

[96] Minhyea Lee, Y. Onose, Y. Tokura, and N. P. Ong. Hidden constant in the anomalous Hall effect of high-purity magnet MnSi. *Physical Review B - Condensed Matter and Materials Physics*, 2007.

[97] J. G. Checkelsky, Minhyea Lee, E. Morosan, R. J. Cava, and N. P. Ong. Anomalous Hall effect and magnetoresistance in the layered ferromagnet Fe14 Ta S2: The inelastic regime. *Physical Review B - Condensed Matter and Materials Physics*, 2008.

[98] N. Kanazawa, Y. Onose, T. Arima, D. Okuyama, K. Ohoyama, S. Wakimoto, K. Kakurai, S. Ishiwata, and Y. Tokura. Large topological hall effect in a short-period helimagnet MnGe. *Physical Review Letters*, 2011.

[99] T. Miyasato, N. Abe, T. Fujii, A. Asamitsu, S. Onoda, Y. Onose, N. Nagaosa, and Y. Tokura. Crossover behavior of the anomalous hall effect and anomalous nernst effect in itinerant ferromagnets. *Physical Review Letters*, 2007.

[100] F. Matsukura, H. Ohno, A. Shen, and Y. Sugawara. Transport properties and origin of ferromagnetism in (Ga, Mn)As. *Physical Review B - Condensed Matter and Materials Physics*, 1998.

[101] R. Adhikari, V. V. Volobuev, B. Faina, G. Springholz, and A. Bonanni. Ferromagnetic phase transition in topological crystalline insulator thin films: Interplay of anomalous Hall angle and magnetic anisotropy. *Physical Review B*, 2019.

[102] S. Iguchi, N. Hanasaki, and Y. Tokura. Scaling of anomalous hall resistivity in Nd2(Mo1-xNbx)2O7 with spin chirality. *Physical Review Letters*, 2007.

[103] Christoph Sürgers, Gerda Fischer, Patrick Winkel, and Hilbert V. Löhneysen. Magnetotransport in ferromagnetic Mn5Ge3,Mn5Ge3 C0.8, and Mn5Si3 C0.8 thin films. *Physical Review B - Condensed Matter and Materials Physics*, 2014.

[104] Qi Wang, Yuanfeng Xu, Rui Lou, Zhonghao Liu, Man Li, Yaobo Huang, Dawei Shen, Hongming Weng, Shancai Wang, and Hechang Lei. Large intrinsic anomalous Hall effect in half-metallic ferromagnet Co3Sn2S2 with magnetic Weyl fermions. *Nature Communications*, 2018.